Dendritic integration in mouse retinal ganglion cells

Dissertation

Zur Erlangung des Grades eines

Doktors der Naturwissenschaften

der Mathematisch-Naturwissenschaftlichen Fakultät

und

der Medizinischen Fakultät

der Eberhard-Karls-Universität Tübingen

vorgelegt

von

Yanli Ran

Aus Chongqing, China

November 2019

Tag der mündlichen Prüfung: .....

Dekan der Math.-Nat. Fakultät: Prof. Dr. W. Rosenstiel
Dekan der Medizinischen Fakultät: Prof. Dr. I. B. Autenrieth

1. Berichterstatter: Prof. Dr. Thomas Euler

2. Berichterstatter: Prof. Dr. Frank Schaeffel

Prüfungskommission: Prof. Dr. Thomas Euler

Prof. Dr. Frank Schaeffel

Prof. Dr. Philipp Berens

Prof. Dr. Aristides Arrenberg

Erklärung / Declaration:

Ich erkläre, dass ich die zur Promotion eingereichte Arbeit mit dem Titel:

“Dendritic integration in mouse retinal ganglion cells”

selbständig verfasst, nur die angegebenen Quellen und Hilfsmittel benutzt und wörtlich oder inhaltlich übernommene Stellen als solche gekennzeichnet habe. Ich versichere an Eides statt, dass diese Angaben wahr sind und dass ich nichts verschwiegen habe. Mir ist bekannt, dass die falsche Abgabe einer Versicherung an Eides statt mit Freiheitsstrafe bis zu drei Jahren oder mit Geldstrafe bestraft wird.

I hereby declare that I have produced the work entitled “Dendritic integration in mouse retinal ganglion cells”, submitted for the award of a doctorate, on my own (without external help), have used only the sources and aids indicated and have marked passages included from other works, whether verbatim or in content, as such. I swear upon oath that these statements are true and that I have not concealed anything. I am aware that making a false declaration under oath is punishable by a term of imprisonment of up to three years or by a fine.

Tübingen, den ....

Datum / Date Unterschrift /Signature

Contents

List of figures

Tables

Abbreviations

AC	amacrine cell
ACSF	artificial cerebral spinal fluid
AMPA	α-amino-3-hydroxy-5-methyl-4-isoxazolepropionic acid
ASD	automatic smoothness determination
BC	bipolar cell
CBC	cone bipolar cell
DLP	digital light processing
DS	direction selectivity
GABA	gamma-aminobutyric acid
GAM	Generalized Additive Models
GCL	ganglion cell layer
HC	horizontal cell
HCN	hyperpolarization-activated cyclic nucleotide-gated
iGluR	ionotropic glutamate receptor
INL	inner nuclear layer
KA	kainic acid
LED	light-emitting diode
mGluR	metabotropic glutamate receptor
NMDAR	*N*-methyl-D-aspartate receptor
OGB-1	Oregon Green BAPTA-1
Oi	overlap index
ONL	outer nuclear layer
OPL	outer plexiform layer
POi	polarity index
PR	photoreceptor
PSP	post-synaptic potential
Qi	quality index
RBC	rod bipolar cell

RF	receptive field
RGC	retinal ganglion cell
ROI	regions of interest
s.d.	standard deviation
SAC	starburst amacrine cell
SARFIA	semi-automated routines for functional image analysis
sOff	sustained Off
SR101	sulforhodamine 101
STRF	spatiotemporal receptive field
tOff	transient Off
TTX	tetrodotoxin
VGluT3 ACs	vesicular glutamate transporter 3 amacrine cells

1 Abstract

Understanding how a neuron integrates the large number of synaptic inputs across its dendritic arbour is critical to understand neural computations. The central nervous system comprises a large variety of neuron types that differ in their morphology, physiology and functional role within the circuit. However, little is known about how cell-type-specific differences in dendritic integration arise from general features such as neuronal morphology and intrinsic membrane properties. Here, retinal ganglion cells, which relay the visual system's first computations to the brain, represent an exquisite model. They are functionally and morphologically diverse yet defined, and they allow studying dendritic integration in a functionally relevant context.

In this thesis, I systematically investigate the dendritic integration of visual information in four types of mouse retinal ganglion cells (transient Off alpha, transient Off mini, sustained Off, and F-mini^{Off}), which receive similar excitatory inputs, but display different visual responses and dendritic morphologies. Using two-photon imaging of dendritic calcium signals from individual cells, and biophysical modelling, I demonstrate that these retinal ganglion cells exhibit diverse type-specific spatio-temporal dendritic integration profiles: In transient Off alpha cells, dendritic receptive fields displayed little spatial overlap, indicating a dendritic arbour that is partitioned in largely isolated regions. In contrast, dendritic receptive fields in the other three cell types overlapped greatly and were offset to the soma in transient Off mini and sustained Off cells, suggesting strong synchronization of dendritic signals likely due to back-propagation of somatic signals. Also, the temporal correlation of dendritic signals varied extensively among these types, with transient Off mini cells displaying the highest correlation across their dendritic arbour. Modelling suggests that morphology alone cannot explain these differences in dendritic integration, but instead specific combinations of dendritic morphology and ion channel densities are required. Together, these results reveal how neurons exhibit distinct dendritic integration profiles, tuned towards their type-specific computations in their circuits and highlight the interplay between morphology and channel complement as a key contributor in shaping dendritic integration.

2 Introduction

In the central nervous system, neurons receive often thousands of synaptic inputs to produce their action potential output (Branco and Hausser, 2010; London and Hausser, 2005; Magee, 2000; Spruston et al., 2016). How these dendritic inputs are integrated may differ between different types of neurons and many properties have been suggested to influence dendritic integration, including dendritic geometry, and complement, distribution and density of passive and active channels as well as synaptic inputs (Branco and Hausser, 2010; Goldstein and Rall, 1974; Lai and Jan, 2006; Stuart and Spruston, 2015). As a consequence, dendritic integration properties can be different between cell types and result in a type-specific relationship between the synaptic inputs and the neurons' outputs. This type-specific input-output relationship of individual neurons is crucial for their functional roles in the whole circuitry (reviewed in (Gulledge et al., 2005; Stuart and Spruston, 2015)).

Dendritic integration has been studied in different classes of cortical neurons, e.g., pyramidal neurons (Cichon and Gan, 2015; Iacaruso et al., 2017), cerebellar Purkinje cells (Finch and Augustine, 1998; Kitamura and Kano, 2013), and retinal neurons, e.g., horizontal cells (Chapot et al., 2017; Grassmeyer and Thoreson, 2017; Vroman et al., 2013), amacrine cells (Ding et al., 2016; Euler et al., 2002; Koren et al., 2017), and retinal ganglion cells (Oesch et al., 2005; Schachter et al., 2010; Schwartz et al., 2012; Sivyer and Williams, 2013). These studies suggest that dendrites can perform complex operations, such as the saturation of synapses (Abrahamsson et al., 2012), the generation of dendritic spikes (Hausser et al., 2000a) and the nonlinearities of N-methyl-D-aspartate receptor (NMDAR) (Major et al., 2013). Such diverse functional operations of dendrites can greatly increase the computational power of single neurons and thus, their circuits. However, it is poorly understood how individual neurons use their specific dendritic properties to integrate information across their dendritic arbour to serve specific computations in the circuits.

2.1 Dendritic integration

A neuron receives most of its inputs along its dendrites. For most central neurons, the dendritic tree is not just summing up individual synaptic inputs, instead, their complex morphology and diverse ion channel complement allow them to perform complex dendritic computations (Behabadi and Mel, 2014; Bernander et al., 1991; Koch et al., 1982; Magee, 2000; Polsky et al., 2004; Williams, 2004). Basically, synaptic inputs onto dendrites alter the influx and efflux of certain ions, leading to the generation of post-synaptic potentials (PSP) that passively propagate to the soma, where, in turn, action potentials (APs) are generated (Fig. 1a; reviewed in (London and Hausser, 2005; Stuart and Spruston, 2015)). If multiple excitatory inputs co-localize in time and space and induce a large depolarization of the membrane beyond the threshold of AP generation, a spike is triggered (Fig. 1b). For example, dendritic spikes have been observed in hippocampus pyramidal neurons while giving multiple synaptic inputs on the same dendritic branch at the same time using two-photon glutamate uncaging (Losonczy and Magee, 2006). Dendritic spikes can remain locally to the dendritic branch in which they initialized and result in local dendritic activities. In this way, individual dendritic branches can function as independent subunits (reviewed in (Branco and Hausser, 2010)). Dendritic spikes can also faithfully propagate to the soma, and trigger more global activities (reviewed in (Connelly and Stuart, 2019; Spruston et al., 2016; Stuart and Spruston, 2015)). Global dendritic spikes may occur if multiple dendritic branches generate dendritic spikes and induce a dendritic depolarization that is sufficiently large to drive the somatic region to initiate APs (Poirazi et al., 2003). APs can both propagate back to the dendritic tree and down to the axon (Fig. 1c). Although it is commonly known that neurons can perform passive and active dendritic integration, it is largely unknown how dendritic integration is shaped by the interplay of type-specific dendritic morphology and ion channel complements.

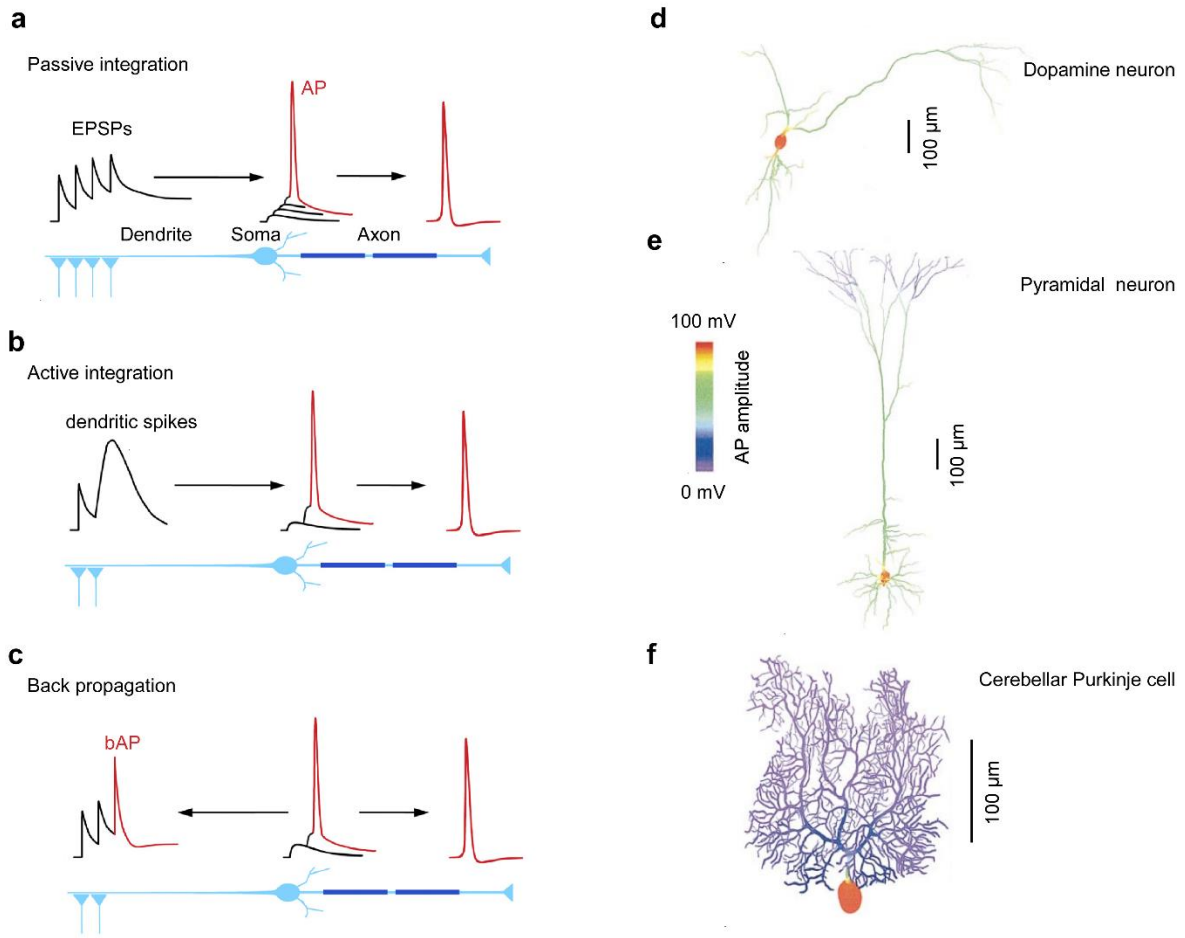

Figure 1 | Action potential initialization and propagation in dendrites.

a, Illustration of passive integration. Synaptic inputs induce excitatory postsynaptic potentials (EPSPs) that propagate to the soma and generate an AP (in red). This AP propagates forward along the axon. **b**, Illustration of active integration. A larger dendritic spike is generated as the result of non-linear integration of synaptic inputs. The dendritic spike propagates to the soma and participates in the generation of AP output. **c,** Backpropagation. An AP (red) generated in the somatic region propagates forward along the axon and backward to the dendritic tree (back-propagating AP, bAP). The bAP interacts with dendritic synaptic inputs. **d-f,** Simulation of APs backpropagation in different morphologies with identical ion channel distributions (Vetter et al., 2001). Substantia nigra dopamine neuron (d), a neocortical layer 5 pyramidal cell (e), and a cerebellar Purkinje cell (f). Panels a-c adapted from a review by (Stuart and Spruston, 2015); panels d-f adapted from Vetter et al.,(2001).

2.1.1 The role of dendritic morphology

The effects of dendritic morphology on the propagation of dendritic APs and PSPs have been investigated by many computational models (e.g.(Jaffe and Carnevale, 1999; Ofer et al., 2017; Vetter et al., 2001)). For example, simulations have shown that in hippocampal pyramidal

neurons, dendritic APs across the long, thick primary dendrites can propagate hundreds of micrometers towards the soma, while in cerebellar Purkinje neurons, which lack long primary dendrites, APs from all dendritic locations propagate less than 100 µm (Vetter et al., 2001). In general, morphological parameters such as dendritic diameter, total dendritic length, total dendritic membrane area, number of dendritic branchpoints and branch density can affect the propagation efficiency of APs in dendrites (reviewed in (Magee, 2000; Stuart and Spruston, 2015)). According to simulations of dendritic AP propagation, however, the most critical morphological parameters determining propagation efficiency are the accumulative change of dendritic diameter across the dendritic arbour, which is mainly determined by the number of dendritic branchpoints, and the change in dendritic diameter before and after branchpoints (Tran-Van-Minh et al., 2015; Vetter et al., 2001). Here, if the dendritic diameter changes less across the dendritic arbour, the propagation of APs is more efficient (Rall and Rinzel, 1973; Rinzel and Rall, 1974; Vetter et al., 2001). Thus, for APs from a given location in the dendritic arbour, the attenuation extent of forward and backward propagation is largely affected by the difference in dendritic diameter between the given sites and the proximal dendrites and the distal dendrites (Katz et al., 2009; Larkum et al., 2009).

2.1.2 The contribution of ion channels

Neural dendrites contain a great number and diversity of ion channels, which modulate the dendritic signals (Stuart and Spruston, 2015; Tran-Van-Minh et al., 2015). For example, in neocortical pyramidal neurons, it has been reported that their thin basal and apical dendrites can generate NMDA receptor-mediated weak Na^+ spikes, but cannot support the generation of Ca^{2+} spikes (Hausser et al., 2000a; Larkum et al., 2009; Spruston, 2008), while their thick apical dendrites can generate global Ca^{2+} spikes (Milojkovic et al., 2005; Nevian et al., 2007). In these neurons, dendritic thickness appears to represent a good predictor of Na^+ or Ca^{2+} spike generation: Thinner dendrites supporting pure sodium spikes, whereas thick dendrites supporting Ca^{2+} spikes, suggesting a differential dendritic distributions of Na^+ and Ca^{2+} channels in pyramidal neurons (Larkum et al., 2009). Since the propagation of dendritic APs largely depends on voltage-gated Na^+ and Ca^{2+} channels (Johnston et al. 1996), the differential distributions of these two channels can result in distinct dendritic propagation properties across

the dendritic arbour. In addition, by modulating the amplitude of dendritic signals, K^+ channels present an important factor determining dendritic propagation in pyramidal neurons (Bikson et al., 1999; Hoffman et al., 1997). Thus, different ion channels play distinct roles in shaping the dendritic integration (Branco and Hausser, 2010; London and Hausser, 2005; Magee, 2000; Spruston et al., 2016).

2.2 Methods for recording dendritic activity

One of the most popular approaches to study dendritic integration is *in vitro* electrophysiology. This approach revealed many fundamental principles of dendritic integration (reviewed in (Stuart and Spruston, 2015)). For example, simultaneous somatic and dendritic recordings from pyramidal neurons (reviewed in (Polsky et al., 2009; Takahashi and Magee, 2009)) as well as from specific types of RGCs (Oesch et al., 2005; Velte and Masland, 1999) have demonstrated that dendrites can initialize APs which efficiently propagate to the soma. In addition, dendritic patch-clamp recordings reveal the dendritic distribution and functional roles of ion channels in different cell types. For example, patch-clamp recordings have demonstrated that neocortical and hippocampal pyramidal neuron dendrites possess voltage-gated Na^+ channels and hence can generate (dendritic) Na^+ spikes (Larkum et al., 2009; Spruston, 2008; Stuart and Sakmann, 1994), while cerebellar Purkinje cell dendrites lack voltage-gated Na^+ channels (Stuart and Hausser, 1994).

While patch-clamp recordings of dendritic activity are very informative, because they report the local electrical activity with a high temporal resolution, such recordings are technically rather challenging and are usually only successful in thick dendrites. Here, imaging dendritic signals using two-photon microscopy largely improves the spatial resolution of dendritic recordings and makes it possible to functionally image subcellular structures including individual spines (Yuste and Denk, 1995). During the last few years, many studies investigated dendritic integration principles by imaging Ca^{2+} signals in individual spines (e.g. (Iacaruso et al., 2017; Jia et al., 2014; Sun et al., 2016)), and revealed, for instance, that Ca^{2+} signals were clustered within individual branches over approximately 10 µm in motor cortex pyramidal neurons of mice while they performing a tactile decision task (Kerlin et al., 2019). Another advantage of using

fluorescence-based (two-photon) imaging is the possibility of obtaining complete dendritic morphologies as a basis for computational modelling and/or to anatomically identify the recorded neuron type. However, limitations of the imaging approach are, for instance, that the imaging depth in scattering biological tissue is limited by the signal-to-background ratio (SBR) (Ouzounov et al., 2017; Theer and Denk, 2006). For *in vivo* two photon-imaging of neural activities, the image depth is normally less than 1mm (Ouzounov et al., 2017; Theer and Denk, 2006). Thus, the imaging of dendritic activities across the dendritic arbour of neurons in the brain *in vivo* is challenging.

2.3 The retina as a model system for studying dendritic integration

Visual processing begins at the retina. In vertebrates, the retina deconstructs the visual signal into ~40 feature-specific parallel channels (reviewed in (Baden et al., 2018)), which are relayed to the brain by a matching number of RGC types (reviewed in (Baden et al., 2018; Sanes and Masland, 2015)). This information processing can be studied in detail in an accessible *in vitro* preparation, keeping the retinal circuits, as well as, the responsiveness to its natural stimulus (light) intact (Ames and Nesbett, 1981). In addition, the retina is structurally and functionally organized in multiple layers with well-characterized cell types and circuits (Fig. 2). Here, the incoming light is detected and transduced by cone and rod photoreceptors, which connect to bipolar cells (BCs) in the outer retina. Then BCs relay the visual information to RGCs, which generate APs for transmission to the brain. In the outer retina, light information from photoreceptors to BCs is modified by horizontal cells (HCs). In the inner retina, neural transmission from BCs to RGCs is modulated by amacrine cells (ACs) by both pre- and postsynaptic inhibition. In addition to this clear input-output relationship, high-resolution 3D morphology for most retinal neurons is available from different EM datasets (Bae et al., 2018; Helmstaedter et al., 2013). This has resulted in a good understanding of type-specific morphology and synaptic connectivity (Bae et al., 2018; Behrens et al., 2016).

Taken together, the retina allows us to study dendritic integration in different cell types, with distinct morphologies in a functionally relevant context. Before I summarize the state of the art

of dendritic integration in the retina, I will give a short overview of the retina's functional organisation.

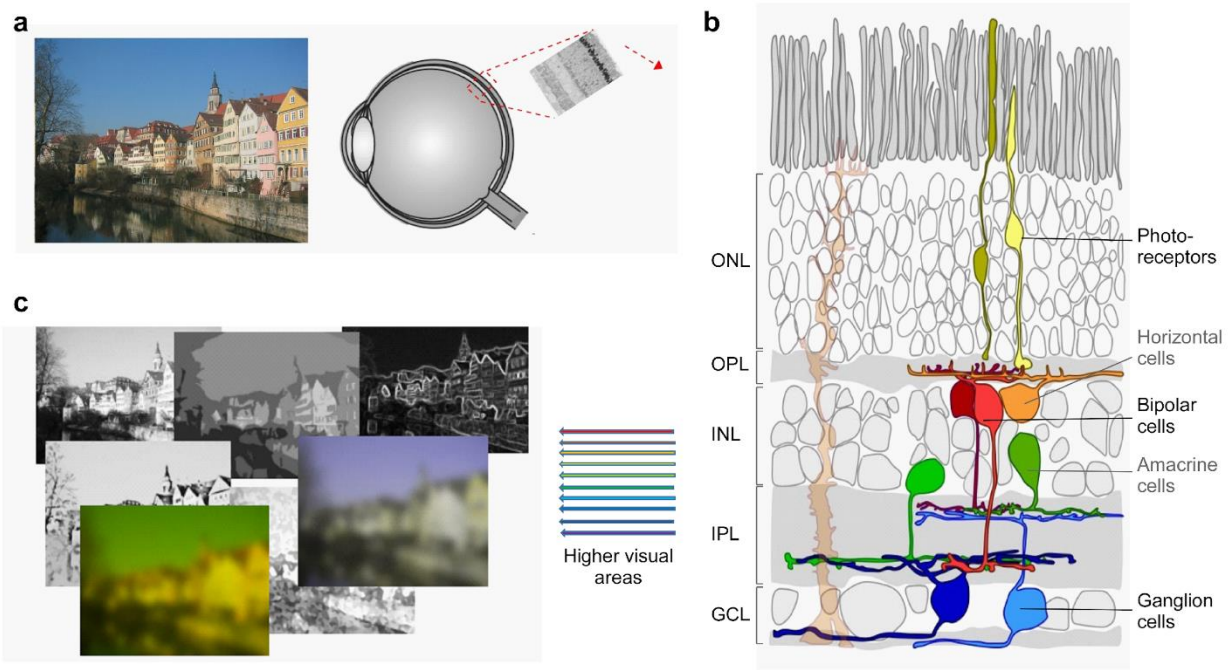

Figure 2 | Pre-processing of visual information in the retinal circuitry.
a. An image is projected onto the retina located at the back of the eye. **b.** Anatomical illustration of the retina. Light enters the retina at the side of the retinal ganglion cells, is transduced by the rod and cone photoreceptors into electrical signals and then fed into the dendrites of bipolar cells in the outer plexiform layer (OPL). In the OPL, horizontal cells modulate the transmission from photoreceptors to bipolar cells by providing lateral feedback. Visual information from bipolar cells is transmitted to the dendrites of retinal ganglion cells in the inner plexiform layer (IPL). Here, both the presynaptic and postsynaptic side can make synapses with amacrine cells and receive modulation from them. **c.** Illustration of a few different visual features extracted by the retinal circuitry, such as contrast, edges or colour, are extracted by the retinal circuitry and these parallel representations are sent to the higher visual areas in the brain. ONL, outer nuclear layer; INL, inner nuclear layer; GCL, ganglion cell layer.

2.4 The functional organization of the retina

In the retina, visual information is processed by cells located in different layers (Fig. 2). In the outer retina, photoreceptors transform the incoming light pattern over space and time into

graded electrical signals by using an opsin transduction cascade (reviewed in (Korenbrot, 2012)). Then, these spatio-temporal signals are transmitted to around 12-15 types of BCs (in mice: 14 BC types; (Franke et al., 2017; Helmstaedter et al., 2013)). In the inner retina, the activated BCs release glutamate to provide excitatory inputs to RGCs, which integrate information from upstream circuits and send the extracted visual features to the brain. This information processing is modulated by HCs in the outer retina and ACs in the inner retina.

2.4.1 Signal transduction in the outer retina

In the outer retina, photoreceptors receive light information and transform the received information into electrical signals. There are two types of photoreceptors in the vertebrate retina – cones and rods. Here, rods only make synapses with one type of BCs – rod BCs, while cones make synapses with all types of BCs (Behrens et al., 2016; Helmstaedter et al., 2013). Functionally, previous studies suggest that rods are highly sensitive to light, and thus the rod pathway is necessary for vision under low light levels (scotopic vision) (Altimus et al., 2010; Schneeweis and Schnapf, 1995). In contrast, cones are activated at higher light intensities and thus the cone pathway contributes to visions during daylight (photopic vision) (Lall et al., 2010). In the following, I will focus on the cone pathway.

In addition to being sensitive to higher light intensities, cones are chromatically selective due to their opsin-expression gradients across the retina. Primates, including humans, are trichromatic with three types of cones expressing specific opsins sensitive to short (S, “blue”), medium (M, “green”) and long (L, “red”) wavelengths of light at approximately 425 nm, 530 nm, and 560 nm, respectively (Riggs and Whittle, 1967). Here, “blue” cones are lacking in the central fovea, while the other two types of cones are distributed across the whole retina (Roorda and Williams, 1999). However, many other mammals including mice, are dichromatic, as they lack the “red” opsin. In the mouse retina, “green” and “blue” cones are most sensitive to light wavelengths at 508 and 360 nm, respectively (Nikonov et al., 2006). In mice and some other mammals, “blue” and “green” cones distribute differentially from dorsal to ventral retina, with “blue” cones primarily in the ventral retina but “green” cones dominant in the dorsal retina (Baden et al., 2013b; Haverkamp et al., 2005; Röhlich et al., 1994; Szél et al., 1992). This distribution of the

"blue" and "green" cones along the dorso-ventral axis has been suggested to serve parallel achromatic channels. For instance, in mouse, functional S-cones in the ventral retina mainly detect visual information from the sky and prefer dark contrasts, while M-cones in the dorsal retina observe the ground and encode bright and dark contrasts linearly (Baden et al., 2013b).

Therefore, in the outer retina, different photoreceptor types present distinct selectivity for light intensity and colour information. This visual selectivity is relayed to BCs for downstream visual processing.

2.4.2 Visual processing in the inner retina

Visual information from the outer retina is relayed to RGCs by BCs in the IPL. Here, BCs not only contact RGCs but also make synapses with ACs. In addition, ACs also make synapses with other ACs and RGCs. The complex interaction between RGCs, BCs and ACs further decomposes the visual information. Cells depolarize and hyperpolarize upon the light in the inner (On layer) and outer (Off layer) part of the IPL, respectively. Both of the On layer and Off layer can be further divided into a number of sub-layers ("strata") where cells exhibit distinct light response properties (Baden et al., 2013; Kaneko, 1970; Kim et al., 2014).

Visual processing in bipolar cells

The axon terminals of BCs ramify at different depth in the IPL. Whether a BC depolarizes or hyperpolarize upon light depends on the type of glutamate receptors expressed on its dendrites (reviewed in (Brandstatter and Hack, 2001)). Off BCs express two types of ionotropic glutamate receptors (iGluRs): α-amino-3-hydroxy-5-methyl-4-isoxazolepropionic acid (AMPA) and kainic acid (KA), and like PRs, hyperpolarize to light (DeVries, 2000). In contrast, On BCs express metabotropic glutamate receptor 6 (mGluR6) in their dendrites (Masu et al., 1995). The activation of mGluR6 leads to the closure of transient receptor potential cation channel (subfamily M member 1, TRPM1, (Koike et al., 2010)), and therefore inverts the light response polarity and depolarization upon light. Besides the subdivision in On and Off, BCs are further divided into different types based on their functional properties, such as sensitivity to contrast, temporal frequency and wavelength of the light (Awatramani and Slaughter, 2000; Baden et al., 2013a; Breuninger et al., 2011; Euler et al., 1996; Franke et al., 2017; Li and DeVries, 2006). In

the mouse retina, light-evoked glutamate output of all the ~14 BC types have been recently characterized by two-photon imaging throughout the IPL (Franke et al., 2017).

Each type of BC has specific light response profiles and provide type-specific excitatory inputs to the connected RGCs and ACs (Helmstaedter et al., 2013; Roska and Werblin, 2001; Yu et al., 2018). In general, BCs stratifying closer to the IPL borders show more sustained responses, while those stratifying closer to the IPL centre exhibit more transient responses (Baden et al., 2013a). The light responses of BCs can be modulated by ACs (Eggers and Lukasiewicz, 2006; Franke et al., 2017), because BCs express inhibitory receptors, e.g., GABA receptors (Shields et al., 2000) and glycine receptors (Grunert and Wassle, 1993; Sassoepognetto et al., 1994)). ACs often attenuate the excitation of their connected BCs by releasing inhibitory neurotransmitters (reviewed in (Franke and Baden, 2017; Roska and Werblin, 2001)). However, some ACs, such as starburst amacrine cells (SACs) and vesicular glutamate transporter 3 amacrine cells (VGluT3 ACs), also release excitatory neurotransmitters (Lee et al., 2016; Masland, 2005). In addition, some ACs can modulate the BCs' light responses across the IPL. For example, the dopamine AC has effects on the response properties of BCs (Puopolo et al., 2001; Witkovsky, 2004). The complex modulation of the "vertical" retinal pathways by ACs is critical for the generation of diverse excitatory input to RGCs: For instance, it has been shown that blocking GABA receptors reduces the functional diversity of BC glutamate responses (Franke et al., 2017). Thus, BCs relay their own intrinsic light response properties together with the modulation by ACs to RGCs.

Interaction between amacrine cells and retinal ganglion cells

The mouse retina contains more than 45 types of ACs, differing in their dendritic stratification and morphology as well as their neurotransmitters (reviewed in (Diamond, 2017)). Unlike BCs and RGCs, most ACs do not have axons and therefore they use their dendrites to receive inputs and also send outputs (reviewed in (Euler and Denk, 2001)). In the IPL, the diverse group of ACs forms a dense network to modify visual signals along the vertical excitatory pathway. In most cases, ACs release inhibitory neurotransmitters like GABA and glycine to modulate the excitation of their connected BCs and/or RGCs. However, some types of ACs also release a second neurotransmitter, e.g., glutamate and acetylcholine (Lee et al., 2016; Masland, 2005), or

a neuromodulator, e.g., dopamine (Pourcho, 1982; Voigt and Wassle, 1987) and nitric oxide (NO) (reviewed in (Vielma et al., 2012)). Neuromodulators can act in a paracrine manner that is they may also affect cells that are not connected via direct synaptic contacts. For example, as NO diffuses through the tissue, NO-producing ACs can modify the response of RGCs and BCs by regulating the GABA release of other ACs by modulating intracellular cGMP levels (reviewed in (Vielma et al., 2012)). Hence, ACs can provide both direct and indirect modulation to the response properties of cells in the IPL (reviewed in (Franke and Baden, 2017)).

Different modulation in the IPL can be sourced from different AC types. However, our knowledge of the cell-type-specific modulation of RGCs by ACs is very limited due to the large diversity of ACs and their complex dendritic morphology. Studies on individual types of ACs have highlighted the importance of AC's modulation on RGC's signalling. One remarkable example is the role of asymmetric inhibition from starburst amacrine cells (SACs) in the generation of direction selective (DS) responses in DS RGCs (reviewed in (Vaney et al., 2012)). Although most interactions between ACs and RGCs are still not well understood in detail, the richness in the anatomical and functional properties of ACs suggests that they play a crucial role in visual processing by the inner retina's circuitry (reviewed in (Franke and Baden, 2017)).

At a general level, mammalian ACs can be divided by the size of their dendritic field into small field and wide-field ACs, which are glycinergic and GABAergic, respectively. The dendrites of small field ACs stratify usually at multiple IPL layers and provide inhibition "vertically" across different IPL layers (reviewed in (Franke and Baden, 2017)). In contrast, wide-field AC dendrites are often mono-stratified in a specific IPL layer and provide lateral inhibition (reviewed in (Diamond, 2017; Euler and Denk, 2001; Franke and Baden, 2017)). Thus, in a specific IPL depth, inhibition can be provided by different AC types. The dendritic arbour of a single RGC can make inhibitory synapses with different AC types and thus receive different inhibition across its dendritic arbour. For example, transient Off RGCs connect with both GABAergic and glycinergic ACs (Murphy-Baum and Taylor, 2018; Pang et al., 2003). The type-selective connections between ACs and RGCs largely increase the diversity of RGCs' outputs.

The retina's output - Retinal ganglion cells

After processing the information received from BCs and ACs within their dendritic arbour, RGCs send visual information to the brain. An important functional property for classifying RGCs is the organisation of their spatio-temporal receptive field (RF), classically defined as the area of the retina where a small light spot induces a change in a neuron's activity rate. Depending on the responses to the light stimuli presented in the centre of the RFs, RGCs are classified into three basic types: On, Off and On-Off. On RGCs depolarize and spike to an increment in light intensity, while Off RGCs depolarize and spike to a decrement in light intensity. On-Off RGCs depolarize to both increments and decrements in light intensity. Light stimuli presented in the regions surround the RF centre typically evoke responses opposite to that evoked by the light stimuli presented in the centre.

Anatomically, RGCs send their dendrites into type-specific layers in the IPL, RGCs that stratify at the Off IPL layers tend to exhibit Off responses, while those stratify at the On IPL layers tend to exhibit On responses (Fig. 3). RGC types with dendritic stratification in both On and Off layers of the IPL tend to exhibit On-Off responses. Besides the dendritic stratification level, different types also show distinct dendritic arbour sizes, branching patterns, dendritic thicknesses, and dendritic segment lengths. In theory, these distinct morphological properties of different RGC types potentially supports various dendritic integration profiles within RGCs (see below; (Koch et al., 1982; Trenholm et al., 2011; Vetter et al., 2001)).

Early studies classified RGCs in the vertebrate retina into ~20 types (reviewed in (Masland, 2012)). These studies identified On vs. Off, transient vs. sustained RGCs, showing light response properties already present at the BC level. In addition, some RGC types exhibited selectivity for local motion or motion direction, features that were not known to be present in BCs and, hence, should result from network interactions with ACs and/or from the dendritic processing in RGCs. Later studies indeed suggested that these more "complex" RGC responses mainly arise from the selective connectivity between interneurons upstream and the organization of synapses along RGC dendrites. For example, direction selectivity in some RGCs was proposed to mainly result from directionally-tuned synaptic inputs and spatially asymmetric connections with a specific

type of AC (reviewed in(Mauss et al., 2017)). Thus, for quite some time, dendritic integration at the level of the RGCs seemed to do little for retinal processing of visual information and, hence, attracted little attention.

In the last few years, a significant number of RGC types have been discovered. In the mouse retina, the latest functional, anatomical and single-cell gene expression studies classified between 30-47 RGC types, which is 2-3 times the number of BC types (Baden et al., 2016; Bae et al., 2018; Rheaume et al., 2018). This striking increase in functional channels indicates that visual information from BCs to RGCs becomes more diverse than previously thought, which unearthed the old question: Are RGC dendrites really mostly "passive integrators" or do they play a more active role in the generation RGC outputs? How dendritic integration /processing does contributes to the functional properties of RGCs? To address these questions was the main objective of my thesis. Before I dive into my study, however, in the next section I will summarize where in the retina dendritic integration was been mostly studied so far.

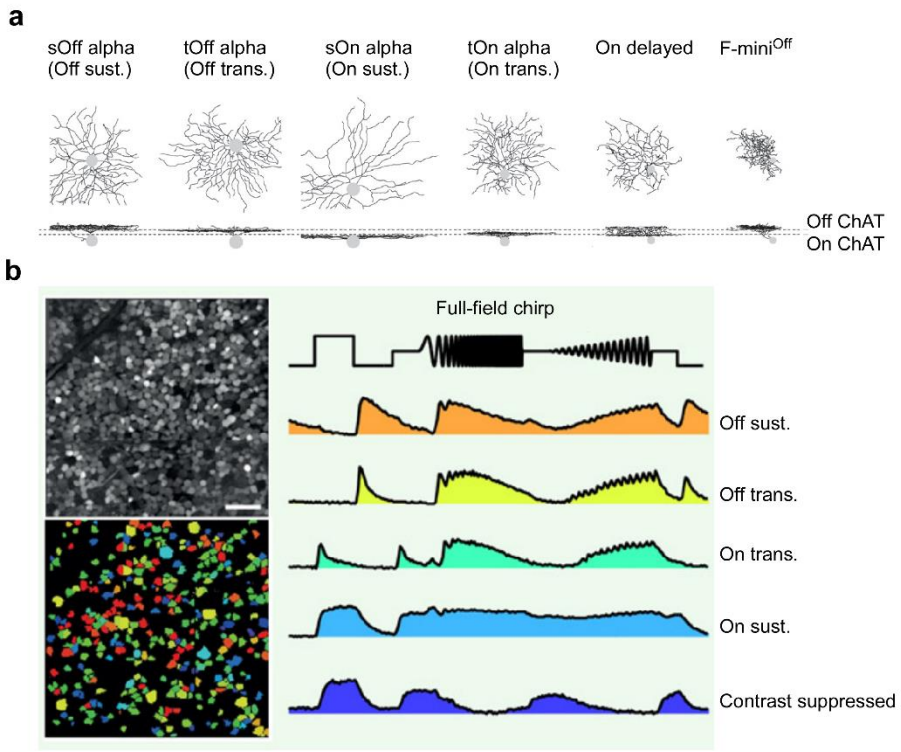

Figure 3 | Morphological and functional differences between retinal ganglion cells.
a, Representative morphologies and IPL stratification depths of different RGC types (Bae et al., 2018). **b**, Population study of RGCs' responses to different light stimuli (Baden et al., 2016). Left top: RGCs in

the whole-mounted mouse retina labelled by electroporation with Oregon Green BAPTA-1; colours (left bottom) indicate functionally clustered different cell types. Scale bar: 50 µm. Right: Ca^{2+} responses of five example cell types to full-field chirp.

2.5 Dendritic integration in retinal neurons

So far, dendritic integration in retinal cells has been mostly studied in interneurons (e.g. HCs, A17 amacrine cells, and SACs) but also to some extent in RGCs. For interneurons, many dendritic recordings have been focused on SACs (e.g. (Euler et al., 2002; Koren et al., 2017; Poleg-Polsky et al., 2018)). For RGCs, dendritic integration has been mainly studied by modelling (e.g. (Borg-Graham, 2001; Schachter et al., 2010; Velte and Miller, 1995)). Experimental evidence for type-specific dendritic integration in RGCs and the biophysical mechanisms remains limited and is restricted to a few big RGC types (e.g. DSGC (Oesch et al., 2005; Sivyer and Williams, 2013), alpha RGCs (Schwartz et al., 2012)).

2.5.1 Interneurons

Previous studies revealed that retinal interneurons can perform complex dendritic computations. In the outer retina, HCs modulate the signal transmission between PRs and BCs across their dendritic arbour (Kemmler et al., 2014; Liu et al., 2013). Recent imaging of light-evoked HC-cone synaptic Ca^{2+} signals revealed that HCs provide local feedback to cones but also relay global feedforward information to BCs (Behrens et al., 2019; Chapot et al., 2017). Reminiscent of the local HC-cone synapse, in the inner retina, A17 amacrine cells provide local feedback to rod BCs (Grimes et al., 2010). For SAC dendrites, which prefer centrifugal light stimuli, compute this direction selectivity by dividing their dendrites into isolated sectors, which contain 15-20 varicosities each (Euler et al., 2002; Koren et al., 2017; Poleg-Polsky et al., 2018). Here, several mechanisms have been forwarded to explain the functional compartmentalization. One proposed mechanism involves a (hypothesized) gradient in intracellular Cl^- concentration, with a higher intracellular Cl^- concentration in proximal than distal dendrites, which results in GABA depolarizing and hyperpolarizing the proximal and distal SAC compartments, respectively (Dmitriev et al., 2012; Gavrikov et al., 2006). Another proposed mechanism for the functional

compartmentalization of the SAC dendrites is the distribution of BC inputs along their dendrites, with input from more sustained BCs close to soma and input from more transient BCs more distally (Ding et al., 2016; Fransen and Borghuis, 2017; Kim et al., 2014; Vlasits et al., 2016). Furthermore, lateral inhibition from neighbouring ACs along SAC dendrites may also contribute to the functional compartmentalization of SAC dendrites (Ding et al., 2016; Lee and Zhou, 2006; Münch and Werblin, 2006).

2.5.2 Retinal ganglion cells

Theoretical studies suggest that RGC dendrites do not simply sum up inputs from BCs and ACs, but instead can carry out complex computations and play an important role in early visual processing. For example, while DS responses in On-Off DS RGCs largely depend on already directionally-tuned, asymmetrically arranged synaptic input from SACs (reviewed in (Mauss et al., 2017)), biophysical models and experimental data suggest a substantial intrinsic contribution resulting from the cell's dendritic morphology: For example, the DS cell's dendritic arbour is divided into independent subunits and generates local dendritic spikes which greatly enhances and sharpens the cell's directional tuning (Oesch et al., 2005; Schachter et al., 2010). In addition, pharmacological data suggest that asymmetries in the dendritic arbour of On-Off DS cells can intrinsically generate DS (Trenholm et al., 2011).

That type-specific dendritic morphology of RGCs may be linked to specific dendritic processing that has been suggested for a long time. A milestone with respect to RGC dendritic processing was a biophysical modelling study by Koch and his colleagues (Koch et al., 1982). They simulated the dendritic electrical properties of different cat RGC types, based on reconstructed morphologies. The authors showed that alpha RGCs which show a large soma, thick primary dendrites, and a large dendritic field, should display spatially inhomogeneous electrical properties, with many independent subunits. In contrast, beta RGCs, with roughly the size of individual alpha RGC subunits, should exhibit rather homogeneous electrical properties. They also modelled other RGC types, including delta and gamma cells, which also suggested type-specific electrical properties. However, so far Koch et al.'s predictions have not been

systematically tested against experimental data, e.g. by measuring dendritic integration across different cell types with distinct dendritic morphologies.

In addition to dendritic morphology, type-specific complements of ion channels also play important roles in dendritic computation. A variety of ion channels have been found in RGC dendrites, including voltage-gated Na^+, Ca^{2+} and K^+ channels, Ca^{2+}-activated K^+ channels and hyperpolarization-activated cyclic nucleotide-gated (HCN) channels, differing in density and dendritic locations between cell types (reviewed in (Van Hook et al., 2019)). These various voltage-gated channels in RGC dendrites enable them to perform active computations. Indeed, dendritic spikes have been observed in alpha and On-Off DSGCs (see above; (Oesch et al., 2005; Sivyer and Williams, 2013; Velte and Masland, 1999)). Here, voltage-gated Na^+, Ca^{2+} and K^+ channels play crucial roles for the generation of dendritic spikes (reviewed in (Bean, 2007; Kampa et al., 2007; Manita et al., 2017; Spruston et al., 2016)). Na^+ and Ca^{2+} channels permit the influx of cations to induce the initialization of dendritic spikes, while the K^+ channels allow the efflux of cations and provide inhibition to the generation of dendritic spikes. Therefore, the specific channel densities and distributions in RGC dendrites can result in distinct dendritic integration properties and thus play different roles in visual processing. For example, in DSGCs, Na^+-based dendritic spikes are essential for the tuning of direction selective responses (Sivyer and Williams, 2013). In Off alpha RGCs, low-voltage-activated (LVA) Ca^{2+} channels are underlying the precisely timed Off response at the offset of light by generating Ca^{2+} spikes at the termination of hyperpolarization (Margolis et al., 2010). However, for many other RGC types, how different ion channels are involved in their visual processing across the dendritic arbour remains largely unknown (reviewed in (Guo et al., 2014)).

In summary, previous studies demonstrated that there are significant differences in dendritic morphologies and ion channel combinations between different RGC types and suggested that these differences may shape dendritic integration in RGCs. However, it is still poorly understood how dendritic integration is shaped by the differences between RGC types in dendritic morphology and ion channel complement.

2.6 The purpose of this study

In this study, I aimed at (i) systematically probing dendritic integration in individual RGCs, (ii) comparing dendritic integration properties between different RGC types, and (iii) exploring the mechanistic principles underlying differences in dendritic integration between different RGC types. For a detailed list of my contributions, see section 10.

(i) To record light-evoked dendritic activity across an RGC's dendritic arbour, I injected a fluorescence Ca^{2+} indicator dye into individual RGCs. To relate dendritic functional features to dendritic morphology, I reconstructed the 3D branching pattern of the recorded cells and extracted morphological parameters, such as the branching order and the dendritic distance from the recording site to soma.

(ii) Dendritic morphology of different RGC types has been well described (e.g. (Bae et al., 2018; Helmstaedter et al., 2013)). To compare dendritic integration between different RGC types, I recorded light-evoked dendritic Ca^{2+} activities in RGC types with distinct morphology and clustered them into different groups depending on their morphological properties.

(iii) To systematically discern the relative contributions of dendritic morphology and membrane properties to the dendritic integration using experimental approaches alone is difficult. Therefore, in this thesis, pharmacology and a morphology-inspired model (contributed by Ziwei Huang) were applied to study the mechanisms underlying dendritic integration in different RGC types.

In conclusion, this study shows that morphologically distinct RGC types exhibit different dendritic integration profiles, which may help them performing specific visual computations. Together, the experimental and modelling data suggest that the interplay of type-specific dendritic morphology and ion channel densities is one key contributor in RGC type-specific dendritic integration.

3 Methods & materials

3.1 Animals

Mice used in this study were purchased from Jackson Laboratory and housed under a standard 12 hour day/night rhythm. For all experiments, both male and female mice aged 5-12 weeks were used. To perform recordings in different types of Off RGC (n=25 animals), I used the transgenic mouse line B6;129P2-Pvalb$^{tm1(cre)Arbr}$/J ('PV', JAX 008069, The Jackson Laboratory; (Hippenmeyer et al., 2005)) cross-bred with the red florescence Cre-dependent reporter line Gt(ROSA)26Sor$^{tm9(CAG-tdTomato)Hze}$ ("Ai9^{tdTomato}", JAX 007905). I also used wild-type mice (C57Bl/6J, JAX 000664, n=3 animals) for alpha RGC recordings as these RGCs can be easily identified due to their large soma size. All animal procedures followed the laws governing animal experimentation issued by the German federal government and were approved by the institutional animal welfare committee of the University of Tübingen.

3.2 Retinal tissue preparation

For all experiments, mice were dark adapted for at least 2 hours. Then, mice were anaesthetized with isoflurane (Baxter) and killed with cervical dislocation. The eyes were quickly enucleated in carboxygenated (95% O2, 5% CO2) artificial cerebral spinal fluid (ACSF) solution containing (in mM): 125 NaCl, 2.5 KCl, 2 CaCl2, 1 MgCl2, 1.25 NaH2PO4, 26 NaHCO3, 20 glucose, and 0.5 L-glutamine (pH 7.4). After carefully removing the cornea, sclera and vitreous body, the retina was flattened on an Anodisc (0.2 µm pore size, GE Healthcare) with the RGC side facing up and then transferred to the recording chamber of the microscope, where it was continuously perfused with carboxygenated ACSF at 35°C (4 ml/min). All experimental procedures were carried out under very dim red light.

3.3 Loading of single cells with calcium indicator

To record light-evoked dendritic signals across single RGCs' dendritic arbour, I loaded Oregon Green BAPTA-1 (OGB-1, hexapotassium salt; Life Technologies, Darmstadt, Germany; 15 mM in

water) into single RGCs. To visualize blood vessels and avoid them when filling individual RGCs, I added 5 µl sulforhodamine-101 (SR101, Invitrogen /Thermo Fisher Scientific, Dreieich, Germany, 50 Mm in water) to per litre ACSF solution. Sharp electrodes with resistances ranging between 70 and 130 MΩ were pulled using a P-1000 micropipette puller (Sutter Instruments, Novato, CA). With a single pulse function (500 ms, -10 nA) of the MultiClamp 900A software, OGB-1 was loaded into individual RGCs. For complete recovery and filling of the injected cells, I started recordings 1 h after injection.

3.4 Local drug application

Electrodes with resistances between 1 and 7 MΩ were used for drug application. Local application of tetrodotoxin (TTX, Tocris, Wiesbaden, Germany, 0.8-1.5 µM, diluted in ACSF) to the soma was performed using a pressure controlled system. To visualize the TTX application, 1 µl of 50 mM SR101 was added to 1 ml TTX solution. Electrodes filled with TTX were positioned directly above the soma of the target cell to guarantee that the flow covered the soma. TTX was applied approximately 1 min before the recordings and lasted until the end of the recordings. After recordings, the region covered by the TTX flow was imaged by taking a z stack from the plane of the electrode to the soma.

3.5 Two-photon imaging and light stimulation

A MOM-type two-photon microscope (designed by W. Denk, MPI, Martinsried; purchased from Sutter Instruments/Science Products) as described previously (Euler et al., 2009) was used for this study. Briefly, the system was equipped with a mode-locked Ti:Sapphire laser (MaiTai-HP DeepSee, Newport Spectra-Physics, Darmstadt, Germany), green and red fluorescence detection channels for OGB-1 (HQ 510/84, AHF, Tübingen, Germany) and SR101/tdTomato (HQ 630/60, AHF), and a water immersion objective (W Plan-Apochromat 20x/1,0 DIC M27, Zeiss, Oberkochen, Germany). For all scans, I tuned the laser to 927 nm, and used a custom-made software (ScanM, by M. Müller, MPI, Martinsried, and T.E.) running under IGOR Pro 6.3 for Windows (Wavemetrics). Time-elapsed dendritic signals were recorded with 64×16 pixel image

sequences (31.25 Hz). High resolution morphology stacks were acquired using 512×512 pixel image stacks with 0.8 or 1 µm z steps.

Light stimuli were projected through the objective lens (Euler et al., 2009). Two alternative digital light processing (DLP) projectors were used for this study: a K11 (Acer, Ahrensburg, Germany) or a LightCrafter E4500 MKII (Texas Instruments, Dallas, TX; modified by EKB Technologies Ltd., Israel). Both were equipped with light-emitting diodes (LEDs) – "green" (576 nm) and UV (390 or 405 nm) that match the spectral sensitivities of mouse M- and S-opsins (for details, see (Baden et al., 2016; Franke et al., 2019)). Both LEDs were intensity-calibrated to range from 0.1 $x10^3$ ("black" background) to 20.0 $x10^3$ ("white" full field) photoisomerisations P*/s/cone. The light stimulus was centred before every experiment, ensuring that its centre corresponded to the centre of the microscope's scan field. For all experiments, the tissue was kept at a constant mean stimulator intensity level for ≥ 15 s after the laser scanning started and before light stimuli were presented.

Light stimuli were generated and presented using the Python-based software package QDSpy (Table 3). Three types of light stimuli were used for this study:

(1) Binary dense noise (20x15 matrix of 30x30 µm pixels; each pixel displayed an independent, balanced random sequence at 5 Hz for 5 minutes) for mapping spatio-temporal RF;
(2) Local (100 µm in diameter) "chirp", consisting of a bright step and two sinusoidal intensity modulations, one with increasing frequency (0.5-8 Hz) and one with increasing contrast as described before (Baden et al., 2016; Franke et al., 2017);
(3) Full-field (800x600 µm) chirp like (2).

3.6 Reconstruction of cell morphologies and extraction of morphological parameters

After recording of dendritic signals, the complete dendritic morphology of single RGCs was acquired using a high-resolution stack. If the cell was not bright enough to see all branch details

after functional recordings, a second microinjection was performed. Using semi-automatic neurite tracing (Longair et al., 2011), I obtained cell skeletons of the recorded RGCs. In cases of any warping of the IPL, as described before (Baden et al., 2016), I de-warped the image stack and corrected the skeletons using custom-written scripts in IGOR Pro.

To cluster the recorded RGCs into different types, the following morphological parameters were extracted using custom-written scripts in IGOR Pro and Python:

(1) *Marginal-central arbour density difference* was calculated using the sum of the dendritic length in central IPL minus the sum of the dendritic length located in marginal IPL as the method used in the study of Bae et al. (2018). To quantify the dendritic stratification of the recorded RGCs in the IPL, I first determined the relative position of the two ChAT bands, the dendritic plexi of the starburst amacrine cells (Vaney, 1984). For this, I used the blood vessel plexi in GCL and the INL as landmarks and defined their positions as 0 and 1, respectively. Then, On and Off ChAT bands corresponded to a relative IPL depth of 0.48 and 0.77, respectively, as shown previously (Baden et al., 2016; Franke et al., 2017).

(2) *Dendritic arbour area* was calculated as the tightest convex hull containing the z-projection of the dendritic arbour.

(3) *Asymmetry* of the dendritic arbour was calculated as the distance between the centre of mass of dendritic density and the soma position.

(4) *Soma size* was defined as the soma area, which calculated from the frame in which the largest area of the soma showed.

To relate dendritic functional properties to the cell's morphology, I registered the relative position of all the recording fields. For each of the recording fields, a region 9 times larger than this recording field was cropped from the reconstructed morphology and z-projected. Next, the recording field was automatically aligned to this cropped region using `match_templates` from *scikit-image* (Table 3). The centre coordinates of all regions of interest (ROIs) in that recording field were then calibrated to the closest dendritic branch based on their Euclidean distance. In rare cases, when automatic matching failed, the matching was done manually.

After aligning the recorded ROIs to the reconstructed morphology, the following parameters were extracted:

(1) *Dendritic distance from ROI to soma.*

(2) *Dendritic distance between ROIs,* defined as the shortest dendritic distance between ROIs (*cf.* Fig. 12a).

(3) *Angular distance between ROIs,* defined as the positive angle between two ROIs and the nearest branching point (*cf*. Fig. 12a).

3.7 Hierarchical clustering

Hierarchical clustering was performed with 1D *k*-means clustering with *k*=2 for all splits, using `KMeans` from the Python package *scikit-learn* (Table 3). First, cells were split into two clusters based on arbour density difference (*cf*. Fig. 8b). Next, the group with lower arbour density difference was separated by soma size, while the group with higher arbour density difference was further split based on their asymmetry index. Here, cells in each group were not slipped further, because they displayed highly consistent light responses. Thus, these four groups were used for further analysis.

3.8 Data analysis

All data were pre-processed using custom-written scripts in IGOR Pro and further analysed in Python and R (Table 3).

*ROIs***:** I extracted ROIs based on dense noise recordings. First, for each recording field, the standard deviation (s.d.) of fluorescence intensity for each pixel over time was calculated to generate an s.d. image of the time-lapsed image stack. In the s.d. image, pixels brighter than mean plus s.d. were defined as dendritic pixels. Second, the time traces of the 100 most responsive dendritic pixels were extracted and correlated with the time trace of every other dendritic pixel in this field. Then for each field, the correlation threshold ($\rho_{\text{Threshold}}$) was determined as the mean of the correlation coefficient (ρ). Finally, I grouped neighbouring pixels (within a distance of 3 µm) with $\rho > \rho_{\text{Threshold}}$ into one ROI.

For each ROI, Ca^{2+} traces were extracted using the image analysis toolbox SARFIA for IGOR Pro (Dorostkar et al., 2010). A stimulus time marker embedded in the recorded data served to align the traces relative to the light stimulus at a temporal resolution of 2 ms. All stimulus-aligned traces together with the relative ROI position on the recorded dendritic arbour were exported for further analysis.

Dendritic RFs: Dendritic RFs were estimated using Automatic Smoothness Determination (ASD, (Sahani and Linden, 2003)), a linear-Gaussian encoding model within the empirical Bayes framework. The relationship between stimulus and response was modelled as a linear function plus Gaussian noise:

$$\mathrm{y_i} = k^T \mathrm{x_i} + \varepsilon_\mathrm{i}, \varepsilon_\mathrm{i} \sim N(0, \delta^2) \quad (1)$$

where x is the binary dense noise stimulus (20x15 matrix of 30x30 µm pixels), y is the gradient of the Ca^{2+} response, k is the spatiotemporal RF (STRF) with time lag ranging from -1000 ms to 0 ms and ε is $i.i.d$ Gaussian noise with zero mean and δ^2 variance.

STRF was then calculated in two steps (Sahani and Linden, 2003):

(1) The ASD prior distribution ($C_{ij} = exp(-\rho - \Delta_{ij}/2\delta)$, where Δ_{ij} is the squared distance between any two filter coefficients) controlled the spatial and temporal smoothness (δ) and scale (ρ), was optimized using evidence optimization.

(2) STRF was then estimated by maximum a posterior linear regression between the response and stimulus using the optimized prior.

The spatial RF maps shown are the spatial component of the single value decomposition of the STRF.

The quality of the spatial RF was determined by the number of contours (at a contour threshold of 0.60), the smallest size of the closed contours and their irregularity degree. The irregularity index was defined as

$$Ii = 1 - \frac{A_{contour}}{A_{convex\ hull}} \quad (2)$$

where $A_{contour}$ is the area of the RF contour, and $A_{convex\ hull}$ is the 2D morphology's convex hull. Only data with a good RF (a single contour with $Ii < 0.1$, $A_{contour} > 1.8 \cdot 1{,}000$ µm^2; see Fig. 5b) were used for further analyses.

Offset between ROI centre and its RF centre: Offset between ROI centre and its RF centre was calculated as the linear distance between the ROI centre and the geometric centre of its RF.

Dendritic RF overlap index: RF overlap index (Oi) was calculated as:

$$Oi = \frac{\mathrm{Ao}}{\mathrm{Amin[A_1,A_2]}} \tag{3}$$

where A_1 and A_2 are RF areas, Ao is the overlap area of A_1 and A_2, and $Amin[A_1, A_2]$ is the smaller area of A_1 and A_2.

Local and full-field chirp: Ca^{2+} traces for local and full-field chirp were linearly interpolated to 500 Hz, baseline-subtracted (mean of 2500 samples before light stimulus) and normalized by the s.d. of the baseline.

Mean traces were calculated using the baseline subtracted traces. To estimate the signal to noise ratio, I calculated the response quality index (Qi) for both local and full-field chirp as the study of Franke et al. (2017):

$$Qi = \frac{\mathrm{Var[\langle C \rangle_r]_t}}{\mathrm{Var[\langle C \rangle_t]_r}} \tag{4}$$

where C is the T-by-R response matrix (time samples by stimulus repetitions) and $\langle\rangle_{\mathrm{x}}$ and $\mathrm{Var}[]_{\mathrm{x}}$ denote the mean and variance across the indicated dimension, respectively. If all trials were identical, the mean response is a perfect representative of the response, $Qi = 1$. If all trials were completely random with fixed variance, such that the mean response is not informative about the individual trials, $Qi \propto 1/R$.

Signal correlation: For the quantification of temporal signal correlation, I only included ROIs with RFs that passed the RF quality test. For some ROIs, the temporal signal quality was relatively low although they showed good RFs, so I repeated the analysis for Qi > 0.4 or 0.5 with comparable result (*cf.* Fig. 16).

Further temporal analysis: Using the responses to the step part of the chirp stimulus, I calculated the transience index (Ti) for local chirp and polarity index POi for both local and full-field chirp. Here only ROIs with Qi > 0.4 were used for the analysis. First, the obtained average traces were binomially smoothed (with 3000 repetitions). Then, 2 s.d. of the baseline (2,500 samples of the smoothed trace before light stimulus onset) were used to determine the time of response onset (T_{R_onset}) and offset (T_{R_offset}).

Ti was calculated as

$$Ti = 1 - \frac{T_{R\_offset} - T_{R\_onset}}{T_{stimulus}} \quad (5)$$

where $T_{stimulus}$ is the stimulus duration.

To calculate the polarity index (POi), data points before and after the response were set to zero, then POi was calculated as:

$$POi = \frac{\sum_{t=0}^{b} r(t+t_{stim\ on}) - \sum_{t=0}^{b} r(t+t_{stim\ off})}{\sum_{t=0}^{b} r(t+t_{stim\ on}) + \sum_{t=0}^{b} r(t+t_{stim\ off})} \quad (6)$$

where b = 3 s. $t_{stim\ on}$ and $t_{stim\ off}$ are the time points of light stimulus onset and offset, $r(t)$ is the mean response at time t. For ROIs responding only to the light-onset, $POi = 1$, whereas for ROIs only responding during the light-offset, $POi = -1$.

3.9 Statistical analysis

Generalized Additive Models (GAMs) were used to analyse the relationships of RF size vs. dendritic distance; RF shift vs. dendritic distance; RF overlap vs. dendritic distance and dendritic angle; correlation vs. dendritic distance and dendritic angle. GAMs extend the generalized linear model by allowing the linear predictors to depend on arbitrary smooth functions of the underlying variables (Wood, 2006):

$$g(\mu) = \beta_0 + f_1(x_1) + \cdots + f_n(x_n) \quad (7)$$

Here, x_i are the predictor variables, g is a link function and the f_i are smooth functions of the predictor variables. These smooth functions can also depend on more than one predictor variable.

In practise, `mgcv`-package for R (Table 3) was used to implement GAMs and perform statistical testing. Here, smooth terms are represented using penalized regression splines. The dependence of the variable of interest as a single smooth term per cell type was modelled for univariate dependencies and a tensor product smooth for bivariate dependencies. The dimension of the basis was set high enough such that the estimated degrees of freedom stayed sufficiently below the possible maximum. Smoothing parameters were selected via the default methods of the package. All models also include a random effect term for cell identity. Typically, models from the Gaussian family were used; for the dependence of RF overlap on dendritic distance and angle, scaled t-distribution was used, as it improved BIC and diagnostic plots.

Statistical significance for differences in the obtained smooths between cell types were performed using the `plot_diff` or `plot_diff2` functions of the `itsdug`-package for R (Table 3). 95% Confidence intervals were calculated using the simultaneous CI-option, excluding the random effect of cell identity.

3.10 Biophysical model

A multi-compartmental 1D model was built to explore the mechanisms underlying dendritic integration in different RGC types. For the model, dendrite thickness and segment length for tOff alpha and tOff mini cells were extracted from published morphologies of "4ow" and "4i" RGCs (*cf*. Fig. 18b), respectively, reconstructed from EM data (http://museum.eyewire.org). Then the medium values of these parameters were mapped to the respective branch order of the model (*cf*. Fig. 18c). The model was implemented in the NEURON simulation environment (Hines and Carnevale, 1997). Here, each dendritic portion (between two branch points) was represented as a "section" in the simulator, which was further divided into multiple "segments" (compartments) with a maximal length of 7 µm. The 1D model can be characterized by the cable equation,

$$\frac{d}{4\tilde{r}_a}\frac{\partial^2 V}{\partial x^2} = C_m\frac{\partial V}{\partial t} + I_{ion} - I_{stim} \qquad (8)$$

where V is the voltage across the cell membrane, x is the distance along the cable, d is the dendritic diameter, $\tilde{r}_a$ is the intracellular resistivity, and C_m is the specific membrane

capacitance. I_{ion} represents the sum of four voltage-gated cation currents (sodium, I_{Na}; calcium, I_{Ca}; delayed rectifier potassium, I_K; A-type potassium, $I_{K,A}$), one calcium-activated potassium current ($I_{K,Ca}$), and one leak current (I_{Leak}). The current dynamics are described following Fohlmeister and Miller (1997) as:

$$\begin{aligned} I_{ion} &= I_{Na} + I_{Ca} + I_K + I_{K,A} + I_{K,Ca} + I_{Leak} \\ &= \bar{g}_{Na} m^3 h (V - V_{Na}) + \bar{g}_{Ca} c^3 (V - V_{Ca}) \\ &+ \left(\bar{g}_K n^4 + \bar{g}_{K,A} a^3 h_A + \bar{g}_{K,Ca}\right)(V - V_K) \\ &+ \bar{g}_{Leak}(V - V_{leak}) \end{aligned} \quad (9)$$

The intracellular stimulation current (I_{stim} in Eq. 8) was the product of a 5,000 ms x 200 µm 1D Gaussian noise stimulus and a BC's spatial RF with a Gaussian shape (with the width set by σ=6 and the centre depends on the current injection location). The stimulation current was injected either at the proximal (at 25 µm from soma) or distal dendrite (at 85% of the total dendrite length from soma), then filtered by a soft rectification function. The magnitude of I_{stim} was scaled between 0 and 15 nA with a mean of 6.17 nA and an s.d. of 1.88 nA to ensure that the input stimulus would elicit spikes in the soma for all parameter combinations.

Model parameters (Table 1) and channel conductances (Table 2) were taken from Fohlmeister and Miller (1997) . Here, different combinations of ion channel densities were grid-searched by multiplying the reference parameters with different scaling factors (for $\bar{g}_K$ and $\bar{g}_{Ca}$, the scaling factors ranged from 0 to 2, and were incremented by 0.25 each step; for $\bar{g}_{Na}$, [0.1, 1, 2] were applied, for $\bar{g}_{K,Ca}$, [10, 100, 1000, 5000, 9000]).

Parameters	**Values**
Temperature	T = 32°C
Intracellular axial resistivity	R_a = 110 Ω·cm
Specific membrane resistance	R_m= 15000 Ω·cm^2
Specific membrane Capacitance	C_m= 1 µF/cm^2
Potassium reversal potential	V_K = -75 mV
Sodium reversal potential	V_{Na}= 35 mV

Table 1 | Model parameters.

Channel type	**Conductance** in [S/cm^2]	
	Soma	Dendrites
$\bar{g}_{Na}$	0.08	0.025
$\bar{g}_{Ca}$	0.0015	0.002
$\bar{g}_K$	0.018	0.012
$\bar{g}_{K,A}$	0.054	0.036
$\bar{g}_{K,Ca}$	0.000065	0.000001

Table 2 | Reference distribution of ion channels in cell compartments

Part	Description (link)	Company /Author	Item number (RRID)
ScanM	2P imaging software running under IGOR Pro	Written by M. Müller (MPI Neurobiology, Martinsried), and T.E.	
IGOR Pro (v6)	https://www.wavemetrics.com	Wavemetrics, Lake Oswego, OR	IGOR Pro v6 (SCR_000325)
Python (v3.6.7)	http://www.python.org/		
R (v2.3)	The R project http://www.r-project.org/		
QDSpy (v0.77)	Visual stimulation software https://github.com/eulerlab/QDSpy	Written by T.E, supported by Tom Boissonnet (EMBL, Monterotondo)	- (SCR_016985)
Scikit-learn (v0.20.0)	Software package for Python	(Pedregosa et al., 2011)	
Scikit-Image (v0.14.2)	Software package for Python	(van der Walt et al., 2014)	
itsadug (v2.3)	Software package for R	(van Rij et al., 2017)	
mgcv (v1.8-24)	Software package for R	(Wood, 2006)	
NEURON (v7.7.0)	Simulation environment for modelling individual neurons and networks of neurons	(Carnevale and and Hines, 2006)	
Custom scripts and data	http://retinal-functomics.net/		

Table 3 | Software used and repositories for custom scripts and data.

4 Results

4.1 Recording dendritic RFs in single RGCs

To record light stimulus evoked dendritic signals across the dendritic arbour of individual cells in the *ex-vivo*, whole-mounted mouse retina, I injected individual RGCs with the fluorescent Ca^{2+} indicator dye OGB-1 using sharp electrodes (Methods). After injection, all dendritic branches of single RGCs were labelled (Fig. 4a) with OGB-1, providing the possibility to image dendritic Ca^{2+} signals across the entire dendritic arbour using a two-photon microscopy (Fig. 4c,d), and to reconstruct the 3D morphology of the recorded cell (Fig. 4b). To determine the cell's dendritic stratification profile across the IPL, blood vessels labelled with SR101 were used as landmarks to define IPL borders and thereby the position of the two ChAT bands (Fig. 4a, b; *cf*. (Baden et al., 2016; Franke et al., 2017) and Methods).

To study spatial dendritic integration properties across the dendritic arbour of individual RGCs, I estimated dendritic RFs in single dendritic segments using a 600x450 µm binary dense noise stimulus centred on the recording field (20x15 pixels, each 30x30 µm; Fig. 4d). For each scan field (32x16 pixels @31.25 Hz; Fig. 4c), I extracted ROIs corresponding to activity units along the dendrites using local image correlations (Fig. 5a; Methods) based on the dense noise recordings. To relate the functional recordings to the cell morphology, I registered the position and distance of each dendritic segment relative to the soma. Then, the Ca^{2+} trace for each ROI was extracted.

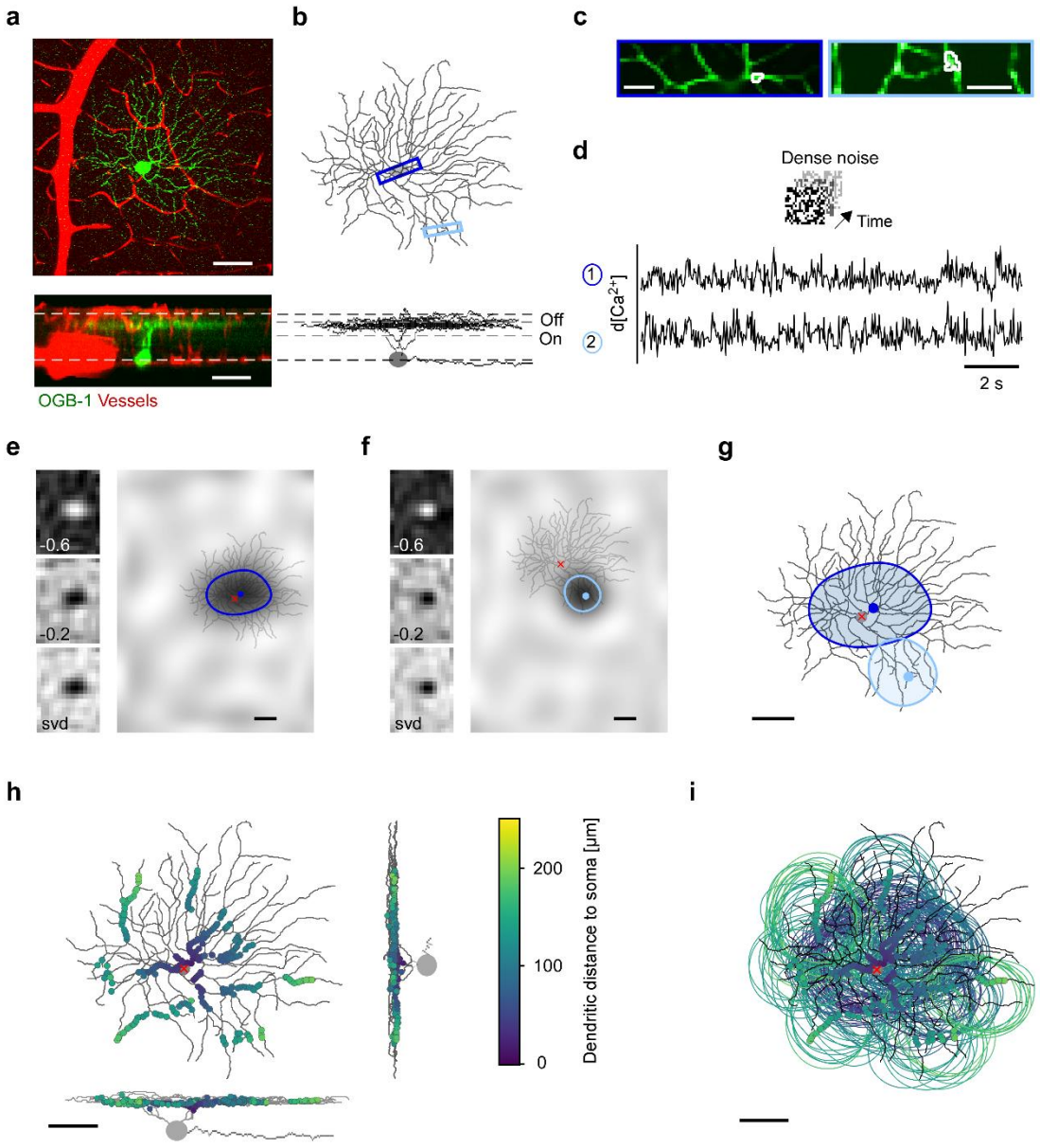

Figure 4 | Measuring dendritic RFs in individual RGCs.

a, Z-projection of an image stack showing an Off RGC filled with the synthetic Ca^{2+} indicator Oregon green BAPTA-1 (OGB-1; green) and blood vessels (red) in top view (top) and as side view (bottom). Dashed white lines mark blood vessels at the borders to ganglion cell layer (GCL) and inner nuclear layer (INL). **b,** Reconstructed morphology of cell from (a). Dashed grey lines between vessel plexi indicate ChAT bands. **c,** Example scan fields, as indicated by blue rectangles in (b), with an exemplary region of interest (ROI; white) each. **d,** De-trended Ca^{2+} signals from ROIs in (c) during dense noise stimulation (20x15 pixels, 30 µm/pixel, 5 Hz). **e,** Spatial RF maps from event-triggered, averaging for left ROI in (c) at different times (δ, [s]), before an event and singular value decomposition (svd; Methods) map (left). Up-sampled and smoothed RF map overlaid with the cell's morphology (right; red crosshair indicates soma position), ROI position (blue dot) and RF contour. **f,** Like (e) but for right ROI in (c). **g,** RF contours of ROIs

from (e, f) overlaid on the reconstructed cell morphology. **h,** Top- and side-view of example cell with all analysed ROIs (n=15 scan fields, n=193 of 232 ROIs passed the quality test; see Methods and Fig. 5b), colour-coded by dendritic distance from soma. **i,** RF contours of ROIs from (h). Scale bars: a,e-i, 50 µm, c, 10 µm.

Using automatic smoothness determination and relevance determination (ASD, Methods), the spatial RF for each ROI was determined (Fig. 4e-g). For the quantification of area and position of each ROI's RF, different thresholds (Fig. 5b; Methods) were used to determine the RF contour for every ROI and its quality. Then, depending on the registered position of each recording field, every ROI with its RF contour was overlaid with the cell´s morphology (Fig. 4e-g). For each cell, I recorded different dendritic regions at various distances from the soma and extracted up to 232 ROIs per cell (Fig. 4h,i; Fig. 9). This allowed me to link spatio-temporal dendritic integration properties across an RGC's dendritic arbour to the morphology and thus systematically probe dendritic integration across the dendritic arbour.

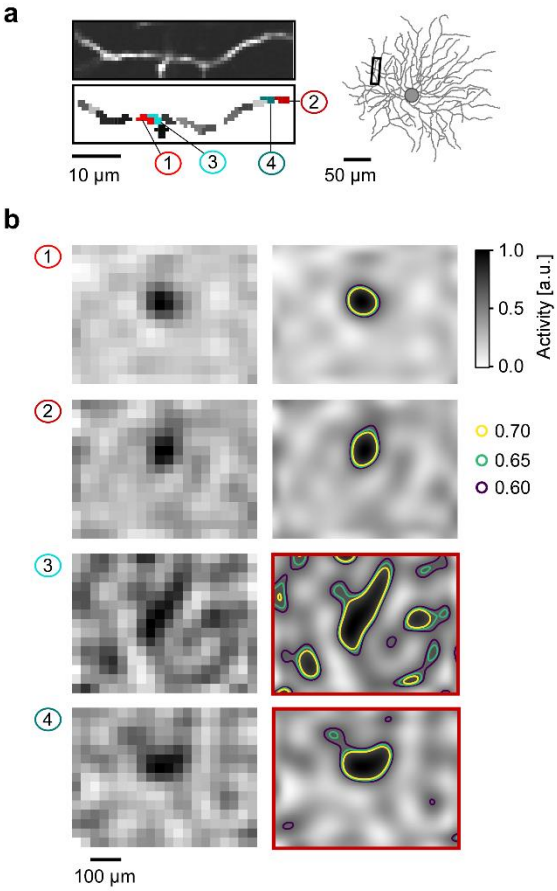

Figure 5 | ROI selection.
a, Exemplary scan field (top left) and automatically generated ROI mask (bottom left) from the region labelled by black rectangle on the reconstructed RGC morphology (right). Red and blue ROIs are shown in (b). **b**, Smoothed and normalized RF maps before (left) and after (right) up-sampling for coloured ROIs shown in (a). Brightness indicates normalized activity. Coloured curves on up-sampled RF maps (right) show RF contours with three different thresholds used for the RF quality test. Only ROIs that passed the test (for details, see Methods) were used for further analysis. Red rectangles around the up-sampled RF maps (right) indicate that RFs did not pass the quality test and were discarded. **c,** Histograms of recorded ROIs for tOff alpha (n=17\850\1,452 cells\total ROIs\ROIs that passed the quality test), tOff mini (n=5\295\387), sOff (n=4\154\208) and F-mini^{Off} RGCs (n=5\126\265).

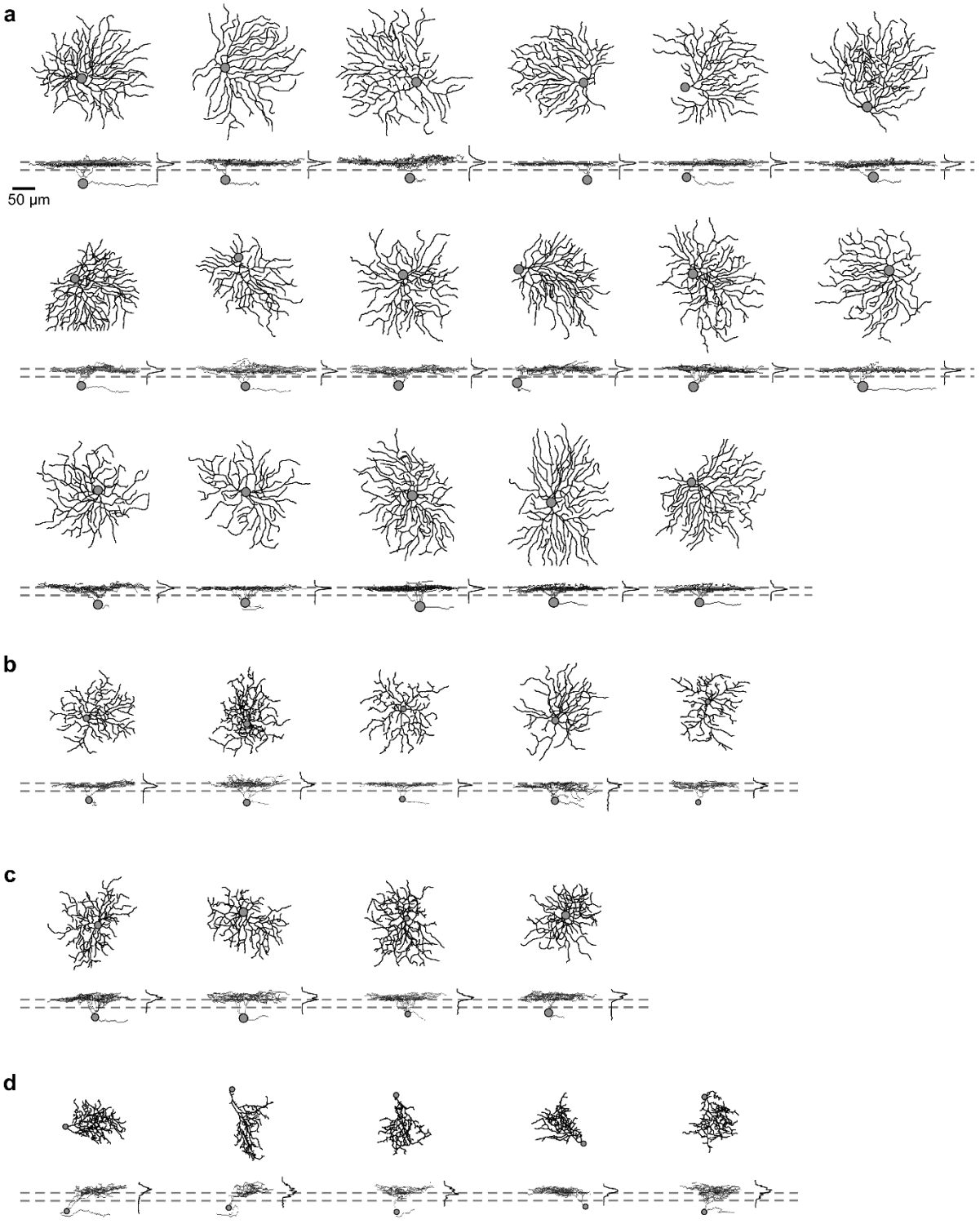

Figure 6 | Morphologies of all recorded RGCs.

a-**d**, Reconstructed morphologies clustered into RGC types using the algorithm published by (Bae et al., 2018): tOff alpha in (a), tOff mini in (b), sOff in (c) and F-mini^{Off} in (d).

4.2 Clustering recorded RGCs into morphological types

To study the dendritic integration rules in different RGCs with distinct morphologies, I recorded the dendritic activity of n=31 Off RGCs (Fig. 6) across their dendritic arbour (Fig. 7a; Fig. 9). Here, to elucidate whether RGCs with similar excitatory inputs use specific dendritic integration rules to generate their specific outputs, I only focused on Off RGCs. After related the RF contours to the dendritic morphology, I observed that dendritic RF patterns differed between different RGCs. For example, in some RGCs, their dendritic RF contours only covered part of the dendritic arbour (Fig. 7a). In contrast, for some other RGCs, their dendritic RF contours seemed to cover almost the whole dendritic arbour area (Fig. 7b).

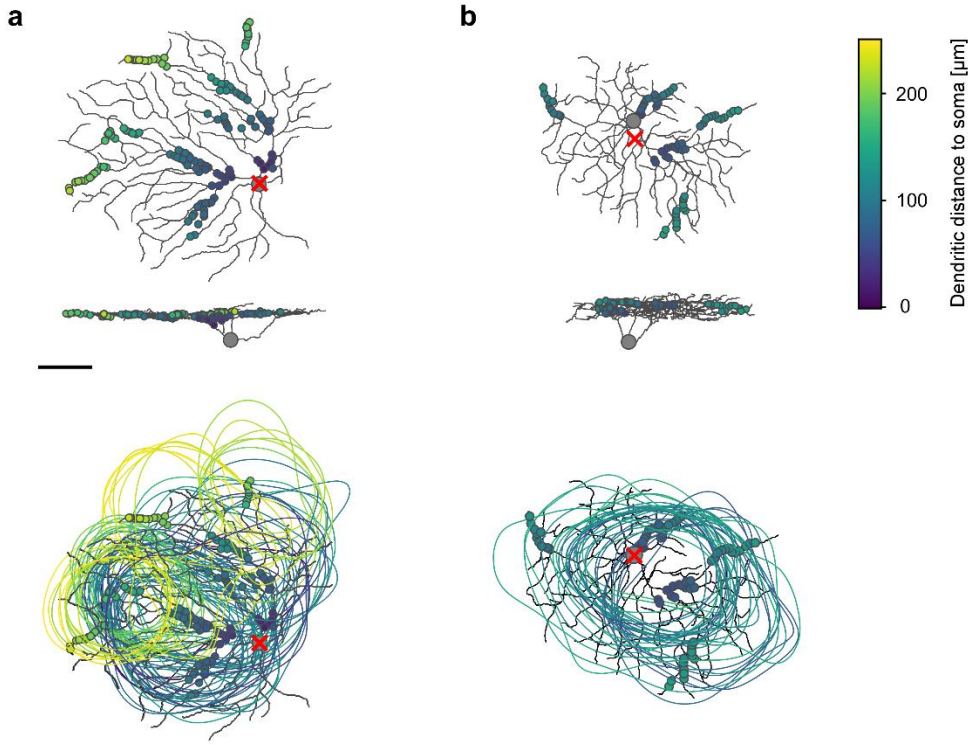

Figure 7 | Recording dendritic RFs in different RGCs.
a, Top- and side-view of a large Off RGC with all analysed ROIs (top) and RF contours of ROIs (bottom; n=9\136\81\scan fields\total ROIs\ROIs passed the quality test), colour-coded by dendritic distance from soma. **b,** Same as (a), but for a smaller cell (n=5\65\34\scan fields\total ROIs\ROIs passed the quality test). Red crosshair indicates the position of the soma. Scale bar: 50 µm.

	n	Arbour density difference (a.u.)	Area (10^3 µm^2)	Asymmetry (a.u.)	Soma size (µm^2)
tOff alpha	17	-2.41 ± 0.44	53.2 ± 2.3	44.9 ± 6.3	322.5 ± 8.3
tOff mini	5	-5.10 ± 0.57	29.7 ± 1.9	18.9 ± 4.1	151.5 ± 14.8
sOff	4	8.58 ± 1.19	29.0 ± 1.5	14.2 ± 3.7	204.0 ± 34.1
F-mini^{Off}	5	6.77 ± 0.62	11.5 ± 0.6	74.8 ± 6.2	102.7 ± 2.2

Table 4 | Morphological parameters describing the dendritic arbours of the clustered RGCs.
For parameter definitions, see Methods.

Thus, the recorded Off RGCs were clustered into different groups based on their morphological properties to compare dendritic integration properties between different morphological RGCs. For the clustering, soma size, arbour asymmetry, arbour density difference, and arbour area (Methods) were extracted from the reconstructed cells (Table 4). Using *k*-means hierarchical clustering (Fig. 8) as described by Bae et al. (2018), the recorded RGCs were clustered into four groups. One group showed larger soma sizes and arbour areas than the other three groups (Table 4). These cells also exhibited large dendritic arbour area, thick primary dendrites, and stratified just below the Off ChAT band, likely corresponding to the classical transient Off alpha (tOff alpha) RGC type (Deny et al., 2017; Krieger et al., 2017; Van Wyk et al., 2009). The second group showed a nearly identical IPL stratification profile to that of tOff alpha cells, but these cells had smaller somata and arbour areas, hence, likely representing the Off "mini" alpha transient (tOff mini) type (Baden et al., 2016). The third group resembled the morphology of F-mini^{Off} cells (Rousso et al., 2016)(Rousso et al., 2016), exhibiting an IPL stratification profile peaking between the Off ChAT band and the INL border, small arbour areas and highly asymmetrical arbours. The fourth group displayed a similar IPL stratification profile as sustained Off alpha RGCs ("1wt" cells in Bae et al., (2018)), but had smaller somata and arbour areas. These cells might correspond to the Off sustained (G_7) RGCs identified in a recent functional study (Baden et al., 2016), and in this study were called sOff (sustained Off). In the following, these morphological groups were referred to as RGC types.

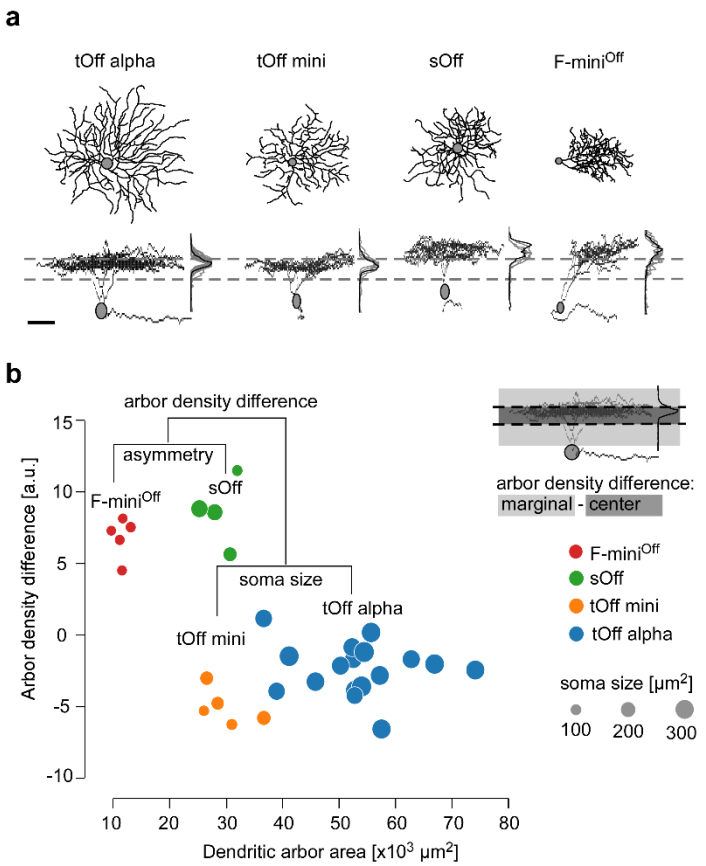

Figure 8| Anatomical clustering of recorded RGCs.

a, Top- and side-views of four reconstructed Off RGCs, one of each studied type, with IPL stratification profiles as mean (black) and for all recorded cells of that type (grey). Dashed lines indicate On and Off ChAT bands. **b**, Cluster-dendrogram with the morphological parameters used in each clustering step and the resulting RGC groups: n=17 tOff alpha, n=5 tOff mini, n=4 sOff and n=5 F-mini^{Off}. Colours indicate cluster (RGC type), dot diameter represents soma area. Inset: Illustration of arbour density difference measure. Scale bar: a, 50 µm.

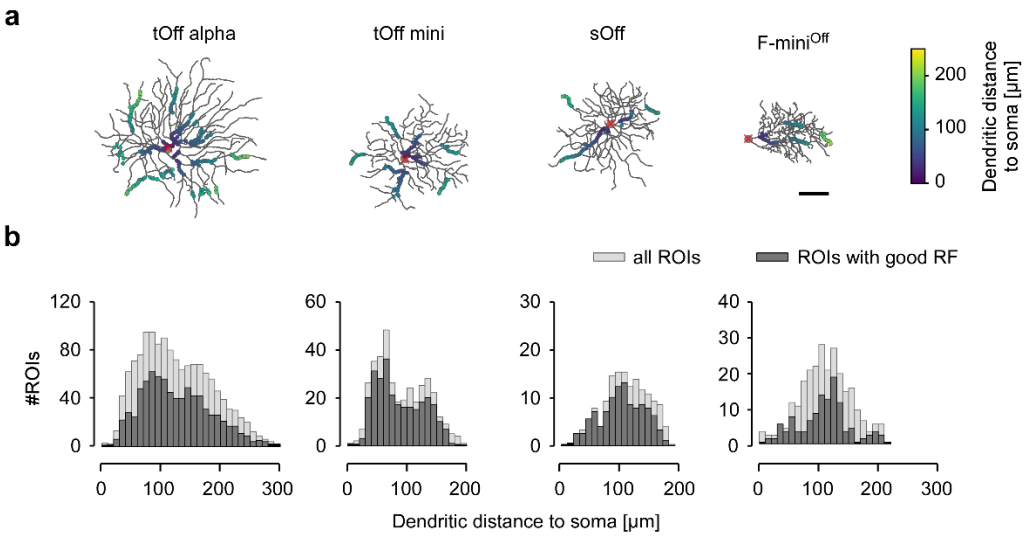

Figure 9 | Number of recorded ROIs for different RGC types.
a, Top-views of the different reconstructed RGC types, overlaid with ROIs that passed the RF quality test. ROI colours indicate dendritic distance to soma. **b,** Histograms of recorded ROIs for tOff alpha (n=17\850\1,452 cells\total ROIs\ROIs that passed the quality test), tOff mini (n=5\295\387), sOff (n=4\154\208) and F-mini Off RGCs (n=5\126\265). Scale bar: a, 50 µm.

4.3 Dendritic RF size differs between RGC types

After relating dendritic RFs to the respective ROI's location in the dendritic arbour, I observed that the change in dendritic RF size along the dendrite in tOff alpha cells was different from that in the other three types (Fig. 10a). The quantification showed that in tOff alpha cells, dendritic RF area decreased as a function of dendritic distance from ROI to the soma (Fig. 10b), suggesting that signals in the distal dendrites of tOff alpha cells are more isolated than those in proximal dendrites. In contrast, RF size did not change significantly with dendritic distance to soma in the other three RGC types (Fig. 10). When dendritic RF size was compared between types, it showed that proximal dendrites in tOff alpha cells exhibited larger RFs than the other types (Fig. 10b; Fig. 13a). These results suggest that dendrites in different RGC types integrate information in different spatial scales.

To investigate the spatial scale of dendritic processing relative to their dendritic arbour, I normalized dendritic RF size to the dendritic arbour area. Normalized RFs were largest and close to 1 for F-mini^{Off} and lowest for distal dendrites in tOff alpha cells (Fig. 10c). Interestingly,

the proximal dendritic segments in tOff alpha showed RF size smaller than 60% of the dendritic arbour area, though they exhibited largest RFs in these four RGC types (Fig. 10c). These differences in normalized RFs between the RGC types suggest the most global dendritic integration in F-mini^{Off} RGCs.

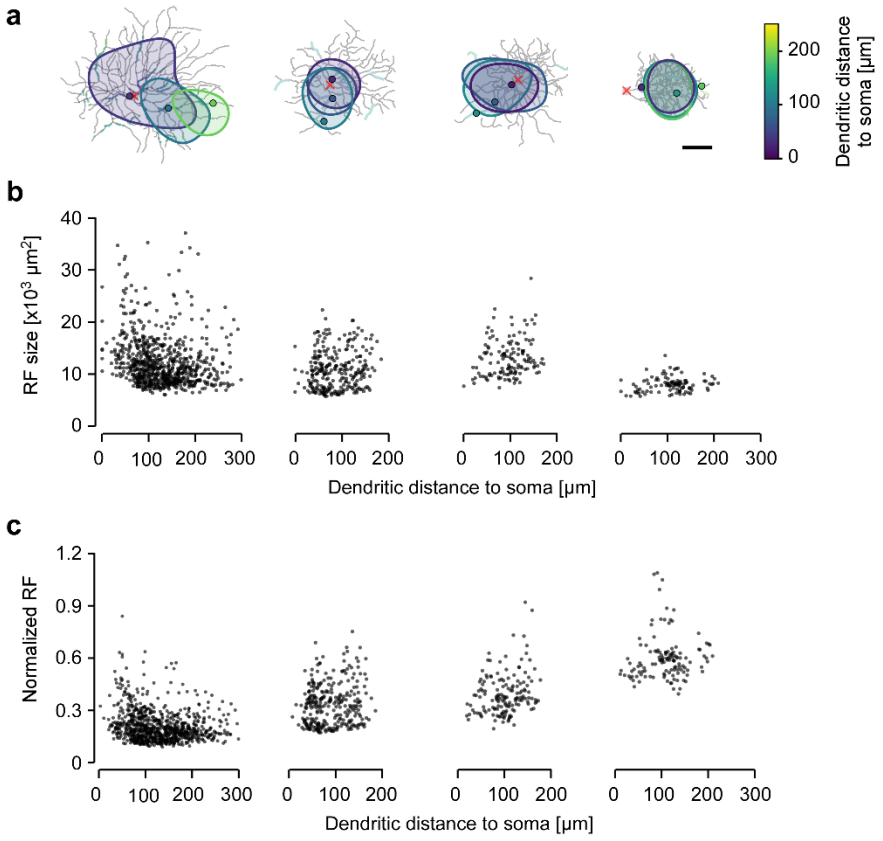

Figure 10 | Local dendritic RF area varies in different RGC types.
a, Cells from (a) with three ROIs of increasing distance from soma and corresponding RF contours overlaid (red crosshair indicates soma position). **b**, Dendritic RF area as a function of dendritic distance to soma; data sampled across cells of the same type (see below). **c**, RF size normalized to the corresponding dendritic arbour area as a function of dendritic distance to soma. Data from tOff alpha (n=17\850\1,452 cells\total ROIs\ROIs that passed the quality test), tOff mini (n=5\295\387), sOff (n=4\154\208) and F-mini Off RGCs (n=5\126\265). Scale bar: a, 50 µm.

4.4 Positions of dendritic RFs varies across RGC types

Dendritic RF offset was calculated to study where the dendritic segments integrate excitatory inputs across the dendritic arbour, which indicated by a vector from a ROI to the geometrical centre of its RF contour (Fig. 11a).

In tOff alpha cells, dendritic segments across the dendritic arbour exhibited small offsets and did not show a systematic change in RF offset with dendritic distance to soma or radial distance to dendritic arbour centre (Fig. 11b,c). In contrast, dendritic RFs were consistently shifted with respect to their recording positions in tOff mini, sOff, and F-miniOff cells (Fig. 11b,c). In tOff mini and sOff cells, RF offset increased with both dendritic distance from ROI to soma and radial distance from ROI to dendritic arbour centre (Fig. 11b,c), Despite this similar trend, distal dendrites in sOff RGCs showed a more pronounced RF offset than those in tOff mini cells (Fig. 13b). For F-mini^{Off} cells, RF offset showed a different trend: Here, all dendritic RFs were shifted towards the dendritic arbour centre (Fig. 11a), resulting in an increasing RF offset with radius distance to soma (Fig. 11c). This trend presents as an inverse bell-curve if the RF offset is plot as a function of dendritic distance to soma (Fig. 11b).

These results suggest that information integration along the dendrites in tOff alpha cells is different from that in the other three types. Dendrites in tOff alpha cells showed local RFs, with larger proximal RFs, suggesting a strong forward propagation (from distal to proximal dendrites). In contrast, in the other three types, dendritic RFs were shifted towards the dendritic arbour centre or the soma (tOff mini and sOff), suggesting a strong backward propagation (from proximal to distal dendrites).

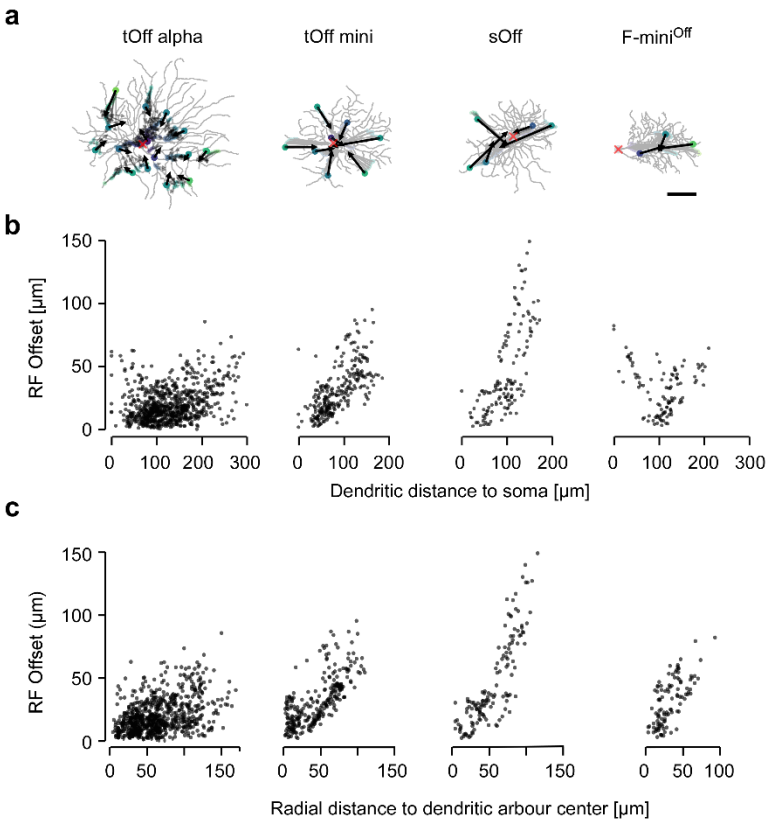

Figure 11 | Local dendritic RF positions varies in different RGC types.
a, Cells from Fig. 9a with arrows indicating spatial offset between ROI centre and the RF contour's geometrical centre, with arrows pointing at the latter. **b**, RF offset of all recorded ROIs as a function of dendritic distance to soma. **c,** RF offset of all recorded ROIs as a function of radial distance to dendritic arbour centre. Data from tOff alpha (n=17\850\1,452 cells\total ROIs\ROIs that passed the quality test), tOff mini (n=5\295\387), sOff (n=4\154\208) and F-mini^{Off} RGCs (n=5\126\265). Scale bar: a, 50 µm.

4.5 Dendritic RF overlap varies across retinal ganglion cell types

The results above revealed small and local RFs in distal dendritic segments of tOff alpha cells, and systematically shifted dendritic RFs, which were shifted towards the soma or dendritic arbour centre in the other three types. These results suggest different spatial relationship between RFs within the same cell. Therefore, overlap among all local RF pairs was determined and overlap maps were generated for the four RGC types (Fig. 12).

In tOff alpha cells, RF overlap index decreased dramatically with increasing dendritic distance and angular distance between ROIs (Fig. 12b). Interestingly, this finding is in line with an early modelling study, which predicted that (cat) alpha RGCs should feature pronounced functional partition (Koch et al., 1982). In tOff mini cells, RF overlap index also decreased with increasing dendritic distance between ROIs, but less pronounced compared to tOff alpha cells. This decrease in RF overlap in tOff mini cells was much less obvious with angular distance (Fig. 12b), suggesting that dendritic distance might be more critical for this change. For sOff and F-mini^{Off} cells, most RFs overlapped substantially, independent of dendritic and angular distance between ROIs (Fig. 12b). As a result, the RF overlap maps significantly differed between tOff alpha and the other three RGC types, and partially between tOff mini and the remaining two RGC types (Fig. 12c; Fig. 13c).

In summary, the results above suggest that the four RGC types exhibit two main different spatial dendritic integration profiles: tOff alpha RGCs feature spatially independent dendrites, with local distal RFs and little RF overlap. In contrast, the other three RGC types have spatially more integrative dendrites, with shifted RFs and large RF overlap across the whole dendritic arbour.

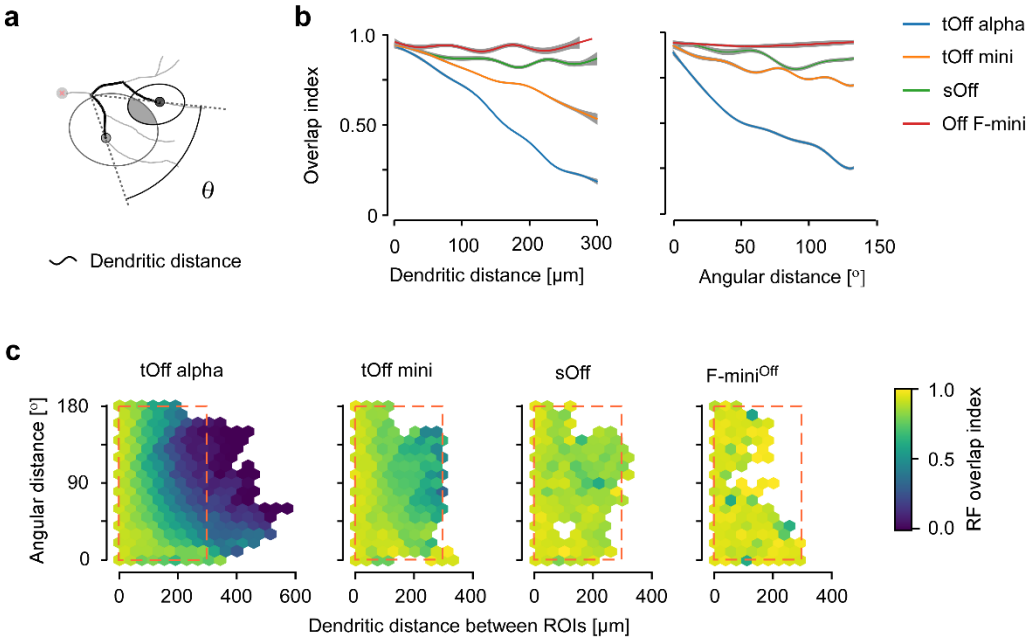

Figure 12 | Dendritic RF overlap.

a, Illustration of dendritic and angular distance (Θ) between two ROIs (measured from the last common branching node) and RF overlap (grey area) of two RF contours (ellipses). **b**, RF overlap index as a function of dendritic distance (left) and angular distance (right) between ROIs. **c**, Hexagon maps showing the dendritic RF overlap index (colour-coded) as a function of Θ and dendritic distance for all ROI pairs: tOff alpha (n=17\40,777 cells\ROI pairs), tOff mini (n=5\13,524), sOff (n=4\3,141), and F-mini^{Off} (n=5\2,097).

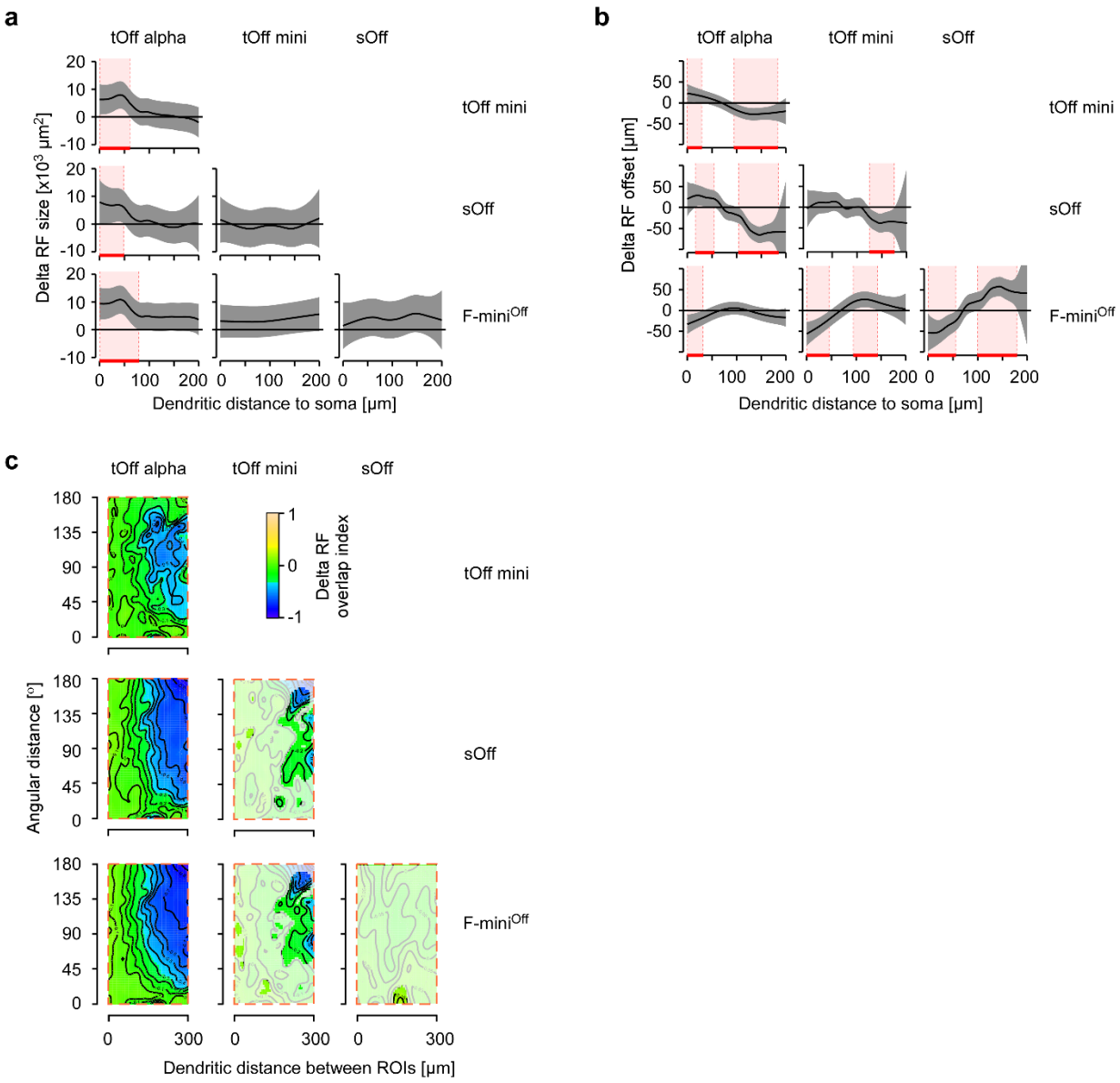

Figure 13 | Statistical comparison of dendritic RFs between different RGC types.
a, Comparison of RF size change with dendritic distance to soma between each pair of RGC type. Red shaded areas indicate dendritic sections with significant differences between types. **b,** Like (a) but for RF offset changes. **C,** 2D comparison maps for dendritic RF overlap for each pair of RGC types. Colour codes for difference in RF overlap index, with whited areas indicating no significant difference.

4.6 Type-specific temporal response features in RGC dendrites

Dendritic inputs are not only integrated over space, but also over time. To investigate temporal dendritic integration properties, I used a “chirp” stimulus that consisted of a light step followed by frequency and contrast modulations. Chirp was presented as local (100 µm in diameters) and full-field (500 µm) version (Methods). To compare spatial and temporal dendritic integration properties, I recorded responses to local and full-field chirp for most of the fields that I recorded dense noise stimulus. This allowed me to use the same ROIs to estimate RFs and analyse temporal responses (Fig. 9; Fig. 14).

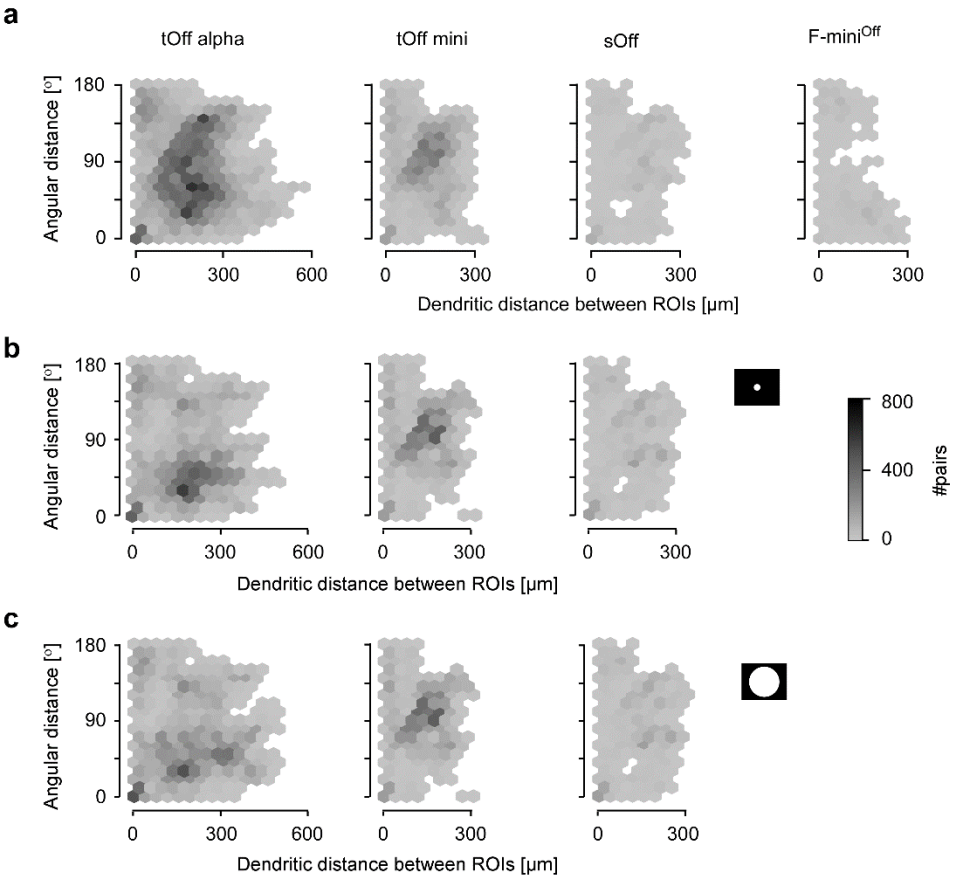

Figure 14 | Number of ROI pairs used for RF overlap and temporal correlation analysis.
a, Hexagon maps showing the number of ROI pairs available for estimation of overlap index in tOff alpha (n=17\40,777 cells\ROI pairs), tOff mini (n=5\13,524), sOff (n=4\3,141), and F-mini^{Off} RGCs (n=5\2,097). **b,c,** Like a, but the number of ROI pairs available for estimation of correlation for local (b) and full-field chirp responses (c). tOff alpha (n=17\12,770\13,001 cells\pairs for full-field\pairs for local), tOff mini (n=5\6,529\6,529) and sOff RGCs (n=4\2,622\2,557).

I found that most ROIs from F-mini^{Off} RGCs did not show reliable responses to local and full-field chirp – although the same ROIs passed the RF quality test, consistent with a previous finding (see x_2 cell in Extended Data Figure 5, Baden et al. 2016). Therefore, F-mini^{Off} cells were excluded for the analysis of temporal response features.

I found that ROIs from tOff alpha and tOff mini RGCs showed similar chirp responses, though they were different from those observed in sOff RGCs (Fig. 15a-c). In general, ROIs from tOff alpha and tOff mini cells showed more transient responses than most of those from sOff cells (Fig. 15e). This finding is in line with the observed differences in stratification profiles (*cf.* Fig. 8a), and therefore differences in their respective BC inputs (Yu et al., 2018): tOff alpha cells receive excitatory inputs mainly from type 3a and 4 BCs, while excitatory inputs of sOff cells mainly from the more sustained type 1 and 2 BCs. Interestingly, in sOff cells, some ROIs also showed highly transient responses to local chirp (Fig. 15e). When comparing response transience along the dendrite, transience index systematically increased with dendritic distance to soma in tOff mini cells for both local and full-field chirp (Fig. 15f). Increasing response transience as a function of dendritic distance to soma was also observed in responses to local chirp in sOff cells, with an even more pronounced change than that observed in tOff mini cells (Fig. 15f). This might be due to the distribution of different BCs along dendrites in these two cell types, with more sustained BC inputs to proximal dendrites but more transient BC inputs to distal dendrites in these two cell types. However, increasing transience index with dendritic distance to soma in sOff cells was not present for responses to full-field chirp, which might be caused by the modification from the surround (Franke et al., 2017). In tOff alpha cells, transience index did not change along dendrites, and there were less pronounced differences between local and full-field chirp responses, compared with that in sOff cells (Fig. 15e,f), suggesting the BCs which contact tOff alpha cells might be evenly distributed along the dendrites.

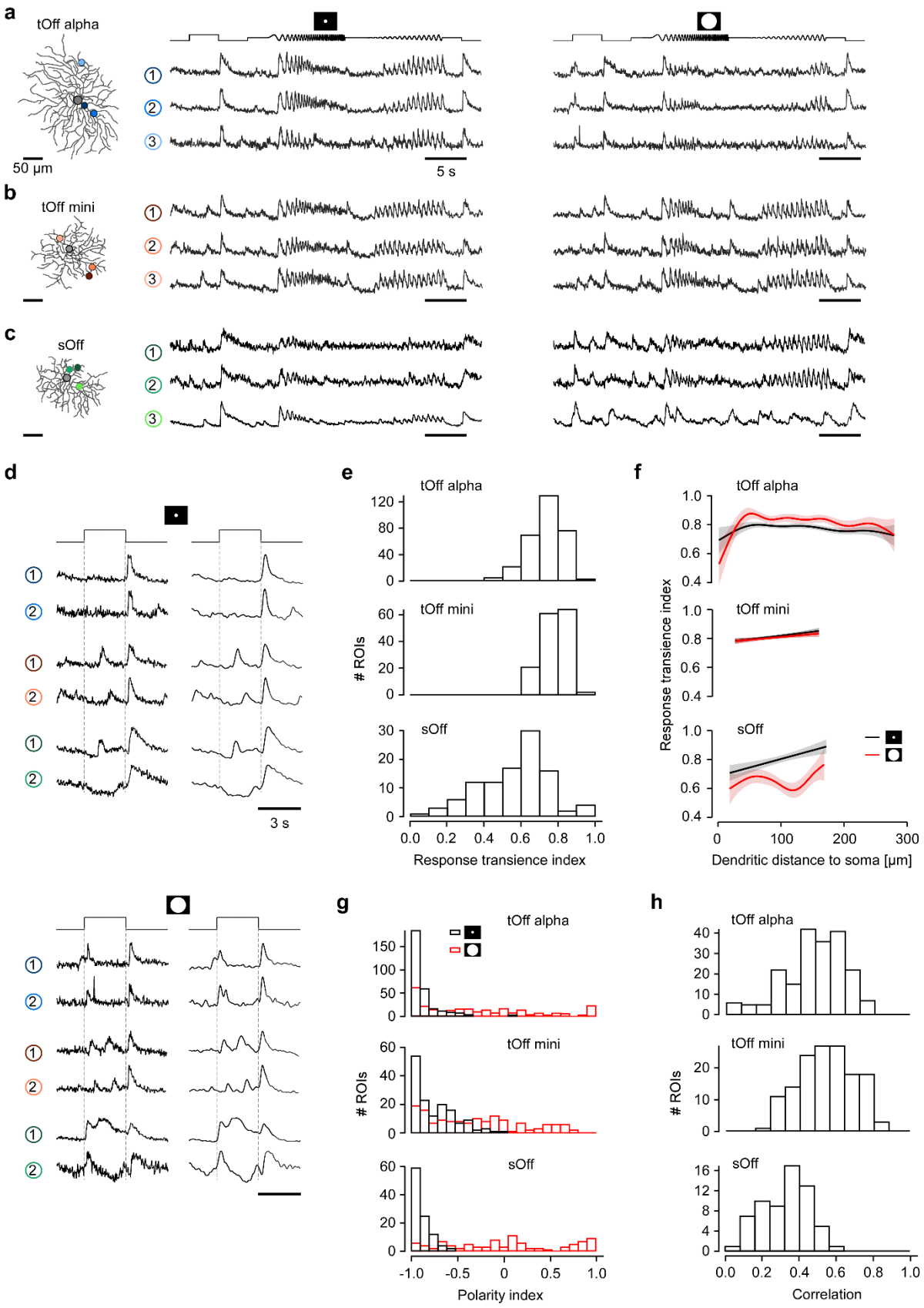
a
tOff alpha
50 µm
5 s
b
tOff mini
c
sOff
d
3 s
e
tOff alpha
tOff mini
sOff
ROIs
Response transience index
f
tOff alpha
tOff mini
sOff
Response transience index
Dendritic distance to soma [µm]
g
tOff alpha
tOff mini
sOff
ROIs
Polarity index
h
tOff alpha
tOff mini
sOff
ROIs
Correlation

Figure 15 | Temporal features of dendritic responses in different RGC types.
a, Exemplary response of a tOff alpha RGC to local (middle) and full-field chirps (right) recorded from three ROIs indicated on the reconstructed cell (left). **b,c**, Like (a), but for tOff mini (b) and sOff RGC (c). **d,** Exemplary responses – unsmoothed and binomially smoothed – to the step section of the local and full-field chirp stimulus. **e,** Histograms of response transience index (Methods) for tOff alpha (n=11\307 cells\ROIs), tOff mini (n=3\148), and sOff RGCs (n=4\103). **f,** Response transience index calculated from the local and full-field chirp responses as a function of dendritic distance to soma. (tOff alpha, n=11\307\282 cells\ROIs for local\ROIs for full-field chirp; tOff mini, n=3\148\146; sOff, n=4\103\93 ROIs) **g,** Like (e), but for polarity index. **h,** Histograms of correlation between local and full-field chirp responses (tOff alpha, n=11\377 cells\ROIs; tOff mini, n=3\ 153; sOff, n=4\129).

Although all these three RGC types stratified their dendritic arbours in the Off layer of IPL, ROIs from these types showed pronounced On events for the full-field chirp that were much less frequent for the local chirp (Fig. 15a-d,g). Similar On event has also been observed in Off BCs (Franke et al., 2017). To quantify the On and Off response component, I used a polarity index (see Methods). The difference in polarity index between full-field and local chirp responses was especially strong in sOff cells (Fig. 15g), resulting in lower correlation of local and full-field chirp responses compared to tOff alpha and tOff mini cells (Fig. 15h). These results suggest that a change in stimulus size has stronger effects on the light responses of sOff cells compared to the other RGC types, likely due to a stronger modulation by the large-scale inhibitory surround.

4.7 Type-specific temporal correlations between RGC dendritic segments

To analyse the temporal correlations between dendritic segments in tOff alpha, tOff mini and sOff cells, I quantified the correlation of local, or full-field chirp responses between ROI pairs across the dendritic arbour of each cell type.

Overall, the correlation for local chirp responses was higher than that for full-field chirp responses in the three RGC types (Fig. 16). This was especially pronounced in sOff cells, with higher correlation of local chirp responses than full-field chirp responses for dendritic distances < 200 µm between ROIs (Fig. 16a,b). In the other two types, the difference in correlation between local and full-field chirp responses was less pronounced than those in sOff cells (Fig. 16).

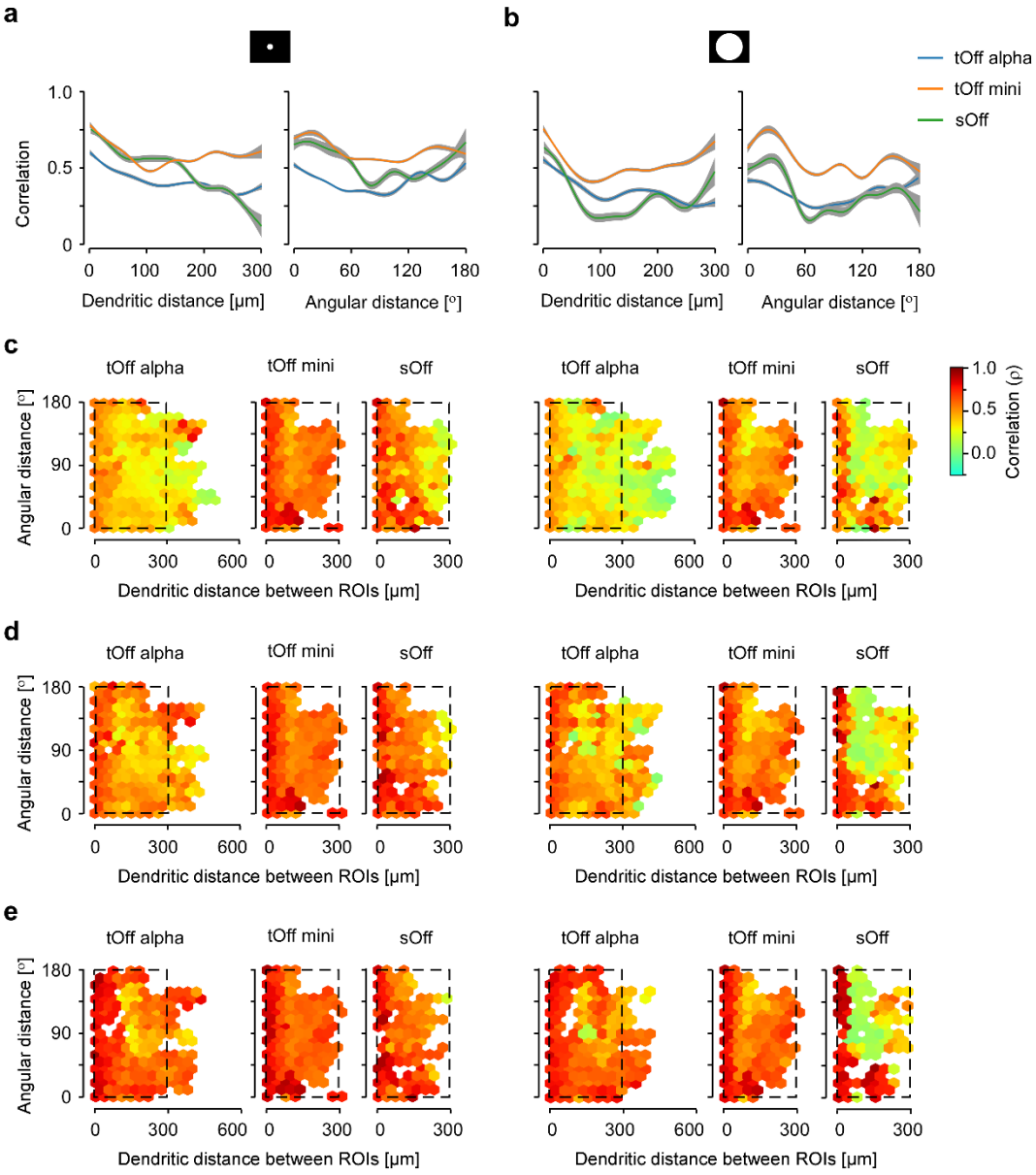

Figure 16 | Temporal correlation across dendrites for different quality thresholds.
a, Response correlations for local chirp as a function of dendritic distance (left) and angular distance (right) between ROIs. **b,** Like (a), but for full-field chirp. **c,** Hexagon maps showing response correlations for local (left) and full-field chirp (right) as a function of angular distance and dendritic distance between ROIs for tOff alpha (n=17\12,770\13,001 cells\pairs for full-field\pairs for local), tOff mini (n=5\6,529\6,529) and sOff RGCs (n=4\2,622\2,557). Colours encoded correlation. **d,e,** Same as (c), but for ROIs with QI>0.4 (d) and QI>0.5 (e).

While comparing temporal correlations between the three types for the same stimulus, I found that correlations in tOff mini cells were much higher than those in the other two types (Fig. 16; 17). This suggests that tOff mini cells have temporally more synchronized dendritic segments, which is in line with their spatially synchronized dendritic segments (*cf.* Fig. 12b,c). For tOff alpha cells, temporal correlation varied substantially across the dendritic arbour but not like the RF overlap index that decreased systematically with increasing dendritic and angular distance between ROIs (*cf.* Fig. 12b,c). Surprisingly, the temporal correlation between dendritic segments in sOff cells varied to a large extent, although they showed large RF overlap for all dendritic segments across the dendritic arbour (Fig. 16).

To confirm that the differences of temporal correlation between cell types were not due to cell-type specific differences in signal-to-noise-ratio, I repeated this analysis for two more stringent quality criteria (for details, see Methods). For both additional quality thresholds, the same correlation differences between cell types were observed (Fig. 16d,e), indicating that temporal correlation differences between RGC types were likely not due to cell type-specific dendritic signal-to-noise-ratios.

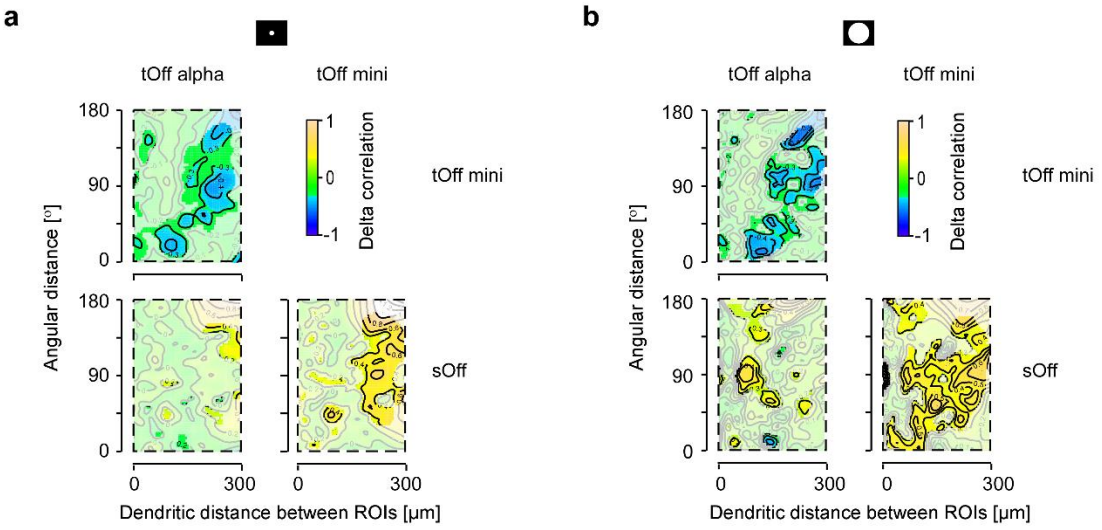

Figure 17 | Comparison maps for temporal correlation.
a, 2D comparison maps for inter-ROI correlation of local chirp responses for data area shown in (Fig. 15c) for each pair of RGC type. Colour codes for difference in correlation, with whited areas indicating no significant difference. **b,** Like (a) but for inter-ROI correlation of full-field chirp responses.

Together, the spatio-temporal data suggest that dendritic integration in RGCs can be tuned to process visual information across their dendritic arbour in a highly type-specific manner, emphasizing different computational modes: for example, highly synchronized dendrites of tOff mini RGCs with overlapping RFs may be specialized for robust detection of visual stimuli independent of their size, while the more independent dendrites of tOff alpha RGCs may rather support high-resolution computations within a single cell.

4.8 Dendritic ion channels together with dendritic morphology contribute to type-specific dendritic integration

After characterizing the type-specific dendritic integration profiles in four Off RGC types, a morphology inspired biophysical model was built to explore the mechanistic principles underlying the different integration profiles. Specifically, how the dendritic morphology and ion channel distribution contribute to dendritic integration. Hence, tOff alpha and tOff mini cells were taken as examples to investigate the mechanistic principles for type-specific dendritic integration. These two cell types showed different dendritic morphology but stratified in the same IPL layer and likely contact the same types of BCs. Thus, the differences in dendritic integration between these two cell types are most likely due to their different dendritic morphology.

For the morphology inspired model, morphological parameters, e.g., dendritic diameter and segment length, were first extracted from a published EM dataset for these two cell types (Bae et al., 2018). In tOff alpha cells, dendritic diameter decreased systematically with increasing dendritic branch order, while this was less pronounced in tOff mini cells (Fig. 18a,b). In addition, dendritic segment length increased with increasing dendritic branch order in tOff alpha, but remained constant in tOff mini. Then, a ball-and-stick model was built based on these morphological differences for tOff alpha and tOff mini cells (Fig. 18c). In this model, dendritic density of Ca^{2+}-activated K^+ channels ($\bar{g}_{k,Ca}$) and voltage-gated K^+, Na^+ and Ca^{2+} channels ($\bar{g}_k$, $\bar{g}_{Na}$ and $\bar{g}_{Ca}$) were systematically varied. For the simulation, either a proximal or a distal input was provided. Based on the observed dendritic integration profiles of these two cell types,

forward propagation should be stronger than backward propagation in tOff alpha cells, while backward propagation should be stronger than forward propagation in tOff mini cells.

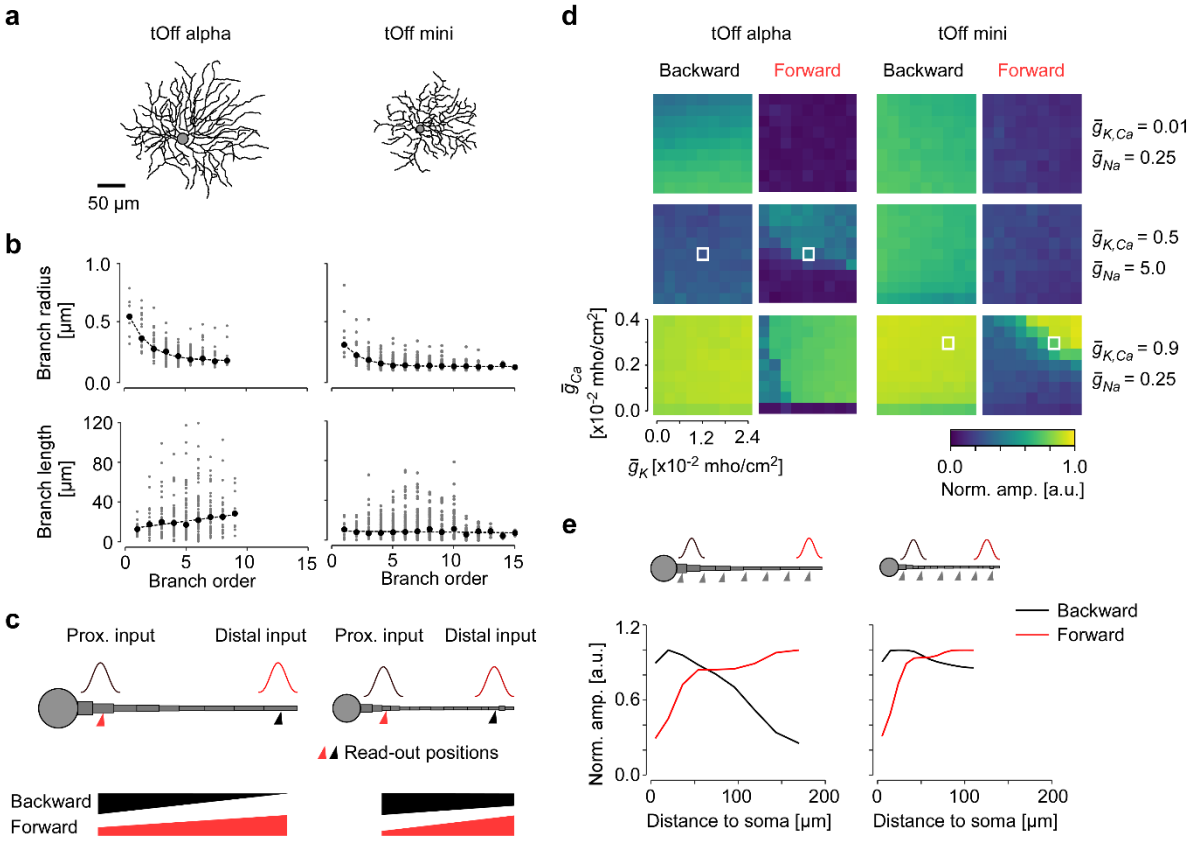

Figure 18 | Simulation of dendritic signal propagation in tOff alpha and tOff mini RGCs.
a, Reconstructed cell morphologies of tOff alpha and tOff mini RGC (same cells as in Figs. 8-11). **b,** Dendrite radius (top) and segment length as functions of branch order (data from http://museum.eyewire.org; n=2 for tOff alpha (4ow); n=3 for tOff mini (4i)). **c,** Illustration of the ball-and-stick models used for simulations in (d, e). Simulated inputs at proximal (25 µm to soma) and distal (85% of the total dendrite length to soma) positions indicated as red and black Gaussians, respectively. Respective read-out positions for (d) are indicated below the dendrite. The thickness change of the bars (bottom) corresponds to the decay of forward (red) and backward (black) signal propagation expected from our experimental data. **d,** Heat maps showing the signal amplitude at the two read-out positions indicated in (c), normalized to the amplitude at the respective input position as a function of ion channel density combinations. White boxes indicate channel combinations that are consistent with our experimental results. **e,** Normalized signal amplitude at read-out positions along the dendrite as a function of dendritic distance for the channel combinations indicated by boxes in (d). Generic voltage-gated ($\bar{g}_{Ca}$, $\bar{g}_K$, $\bar{g}_{Na}$) and Ca^{2+} activated ($\bar{g}_{K,Ca}$) conductances were modelled after Fohlmeister and Miller (1997). For details, see Methods.

The simulation results showed that the same combination of ion channel densities had different effects on signal propagation in the two modelled cells (Fig. 18d; Fig. 19b), suggesting an important role of dendritic morphology in shaping dendritic integration. Notably, type-specific ion channel combinations produced the expected dendritic signal propagation: For tOff alpha cell dendrites, intermediate $\bar{g}_{k,Ca}$ and high $\bar{g}_{Na}$ and $\bar{g}_{Ca}$ channel densities were required to generate stronger forward propagation compared to backward propagation (Fig. 18d; Fig. 19b). For the same channel densities, forward propagation in the modelled tOff mini cell was so low that distal inputs were almost completely extinguished before reaching the proximal dendrite. In contrast, with higher $\bar{g}_k$ and lower $\bar{g}_{Na}$ densities, tOff mini cells showed strong backward and substantial forward propagation, in line with the hypothesis (Fig. 18d; Fig. 19).

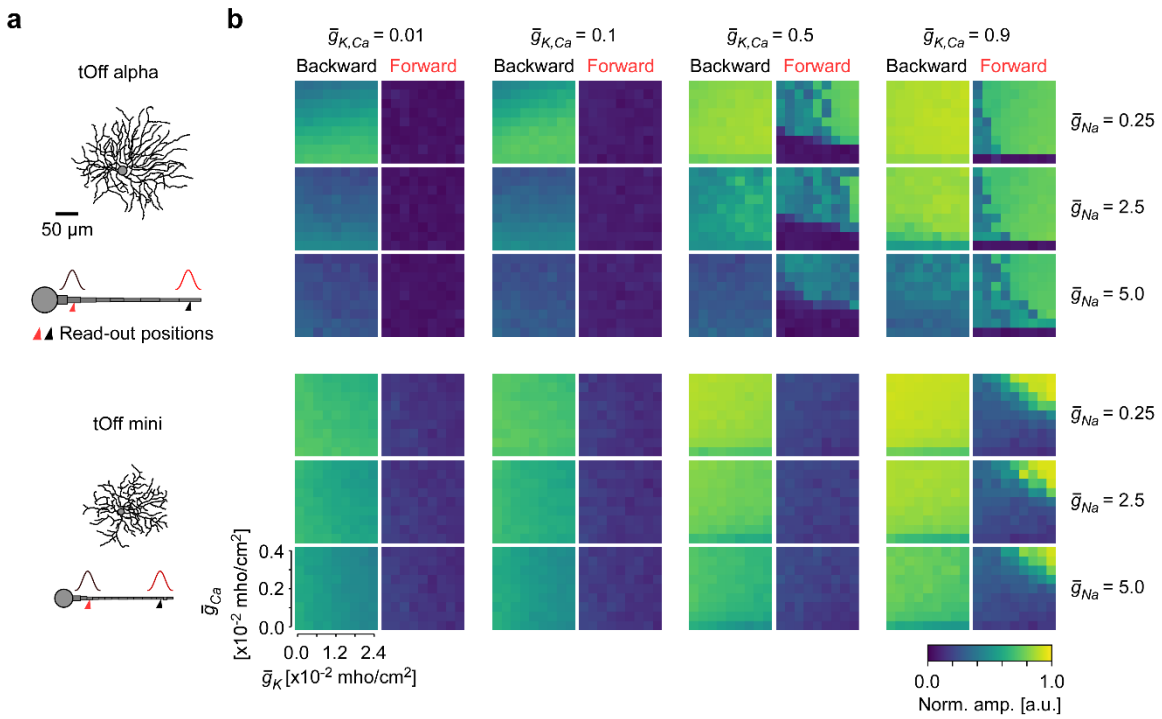

Figure 19 | Simulation of dendritic signal propagation in tOff alpha and tOff mini RGCs.
a, Reconstructed cell morphologies of a tOff alpha and a tOff mini RGC with illustrations of the respective ball-and-stick models (same as in main Figure 6a,c). Simulated inputs at proximal (25 µm to soma) and distal (85% of the total dendrite length to soma) positions indicated as red and black Gaussians, respectively. **b,** Heat maps showing the signal amplitude at the two read-out positions indicated in (c), normalized to the amplitude at the respective input position as a function of ion channel density combinations.

Together, the modelling results showed that passive dendrites – morphological differences alone – could not reproduce the observed dendritic integration properties, while a combination of morphology and active dendrites reproduced the main experimentally observed dendritic integration properties.

4.9 TTX application changes dendritic RFs in tOff alpha and tOff mini RGCs

The experimental and modelling results suggest that back-propagation in tOff mini cells is stronger than that in tOff alpha cells. It has been shown that local application of TTX can suppress the APs at the soma, and thus reduce the effects of somatic APs on the distal dendrites (Huguenard et al., 1989; Regehr et al., 1993). Hence, to pharmacologically test if back-propagation of somatic spikes affect dendritic integration in tOff alpha and tOff mini cells, I locally applied TTX (0.8-1.5 µM) to the soma of the injected cell (Fig. 20a). Then I measured the RFs of proximal dendrites that were covered by the TTX flow, and of distal dendrites located on the opposite side of the TTX flow and therefore not (or little) affected by the drug (Fig. 20b).

I found that the size of proximal RFs in tOff alpha cells did not systematically change upon TTX application (Fig. 20c), whereas it did significantly decrease in tOff mini cells. This suggests the presence of at TTX-sensitive Na^+ channels in the proximal dendrites of tOff mini but not in tOff alpha cells. In fact, previous immunohistochemical data shows that alpha cells express TTX-resistant Na^+ channels, while smaller RGCs do not (O'Brien et al., 2008). It will be interesting to test in future experiments if proximal RFs in tOff alpha RGCs can indeed be altered with respective blockers of TTX-resistant Na^+ channels.

Unlike proximal ROIs, which were always covered by TTX flow, distal ROIs were only partially affected by TTX (Fig. 20a). Thus, when analysing the RF size changes for distal ROIs, I distinguished two cases: Covered by TTX flow or not (Fig. 20c). In both tOff alpha and tOff mini cells, RF size of distal ROIs decreased when covered by the TTX flow (Fig. 20c). Surprisingly, in tOff alpha cells, RF sizes also tended to decrease in distal ROIs that were not covered by the TTX flow (Fig. 20c). It is possible, though, that a low concentration of TTX reached also the parts of the dendritic arbour that – judging from the SR101 fluorescence – was not covered (directly) by the TTX flow. However, why this was not the case for tOff mini cells is unclear. In any case, it interesting that in tOff alpha cells, distal but not proximal RFs ware altered by TTX, as it

indicates that the type of Na^+ channel – TTX-resistant proximal (*cf.* (O'Brien et al., 2008)) and TTX-sensitive distal – may change along the dendrite.

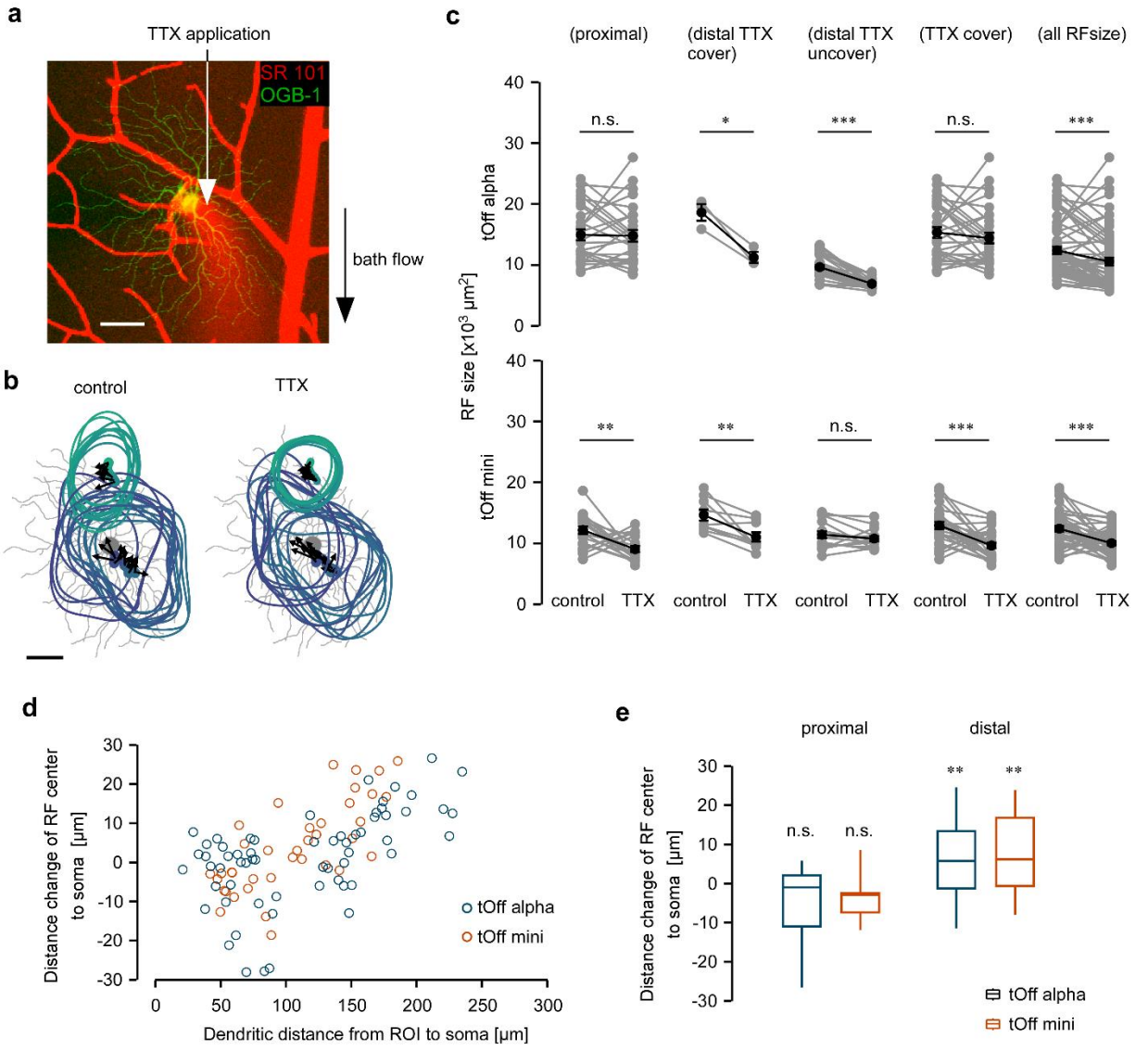

Figure 20 | Effect of TTX application on dendritic RFs in tOff alpha and tOff mini cells.
a, Z-projection of an image stack showing the local application of TTX to the soma of the target cell, with arrows indicating the position of TTX application and the direction of the TTX flow. **b,** RF contours for ROIs indicated by colour dots overlaid with the reconstructed cell morphology, with arrows pointing from the ROIs to their RF geometrical centres. Scale bar: 50 µm. **c,** Dendritic RF size changes with TTX application or without TTX application for proximal, distal and all ROIs recorded in tOff alpha (n=5\27\3\32\30\62\ cells\proximal ROIs\distal TTX covered ROIs\distal TTX uncover ROIs\all TTX covered ROIS\all ROIs) and tOff mini cells((n=3\20\9\15\29\44\ cells\proximal ROIs\distal TTX covered ROIs\distal TTX uncover ROIs\all TTX covered ROIS\all ROIs). **d,** Distance change induced by TTX

application from RF centre to soma as a function of dendritic distance to soma. **e,** Averaged distance change from RF centre to soma for proximal and distal ROIs. Statistics were performed using t-test with alpha=0.05, *p<0.05, **p<0.01, ***p<0.001.

Next, I compared if dendritic RF positions in tOff alpha and tOff mini cells were changed by TTX application (Fig. 20d, e). In both RGC types, RF position of proximal RFs tended to move slightly towards the soma, while for distal dendrites, I observed a shift away from the soma changed significantly. These trends were similar in the two types. This suggests that TTX application affected the interaction between proximal and distal dendrites in these two types.

It is known that TTX does not only affect somatic spikes in RGCs but also can alter the activity of BCs and ACs (Bloomfield, 1996; Cui and Pan, 2008; Kaneko and Watanabe, 2007; Taylor, 1999; Van Wart et al., 2005; Zenisek et al., 2001), which contribute to the excitation centre and inhibition surround of RGCs, respectively. Thus, it cannot be excluded that the observed changes in dendritic RF size and/or position may at least in part due to changes in the upstream circuit, i.e. changes in the centre-surround interaction. Therefore, in the next section, I analysed the effects of TTX application on the centre-surround dendritic signals.

4.10 Effects of TTX application on the centre-surround interaction in tOff alpha and tOff mini RGC dendrites

To determine whether the TTX application affected the centre-surround interaction in the dendrites of tOff alpha and tOff mini cells, I quantified the correlation between the responses to local and to full-field chirps (Fig. 21a). In tOff alpha cells, TTX application decreased the correlation between the local and full-field chirp responses (Fig. 21b), which could indicated that surround inhibition became stronger and which would be consistent with the decrease in the distal RFs of these cells (*cf.* Fig. 20c). Interestingly, the opposite effect was observed for most ROIs in tOff mini cells, where the correlation between local and full-field chirp responses increased upon TTX application (Fig. 21b), possibly due to a decrease in inhibition from the surround. If TTX indeed decreases the surround inhibition in tOff mini, one would have expected that their dendritic RF sizes increase – similar to what has been reported for primate On RGCs, where TTX reduces the surround inhibition of the excitatory inputs and thus increases

their RF size (Protti et al., 2014). However, most ROIs from tOff mini cells exhibited decreased RFs upon TTX application (*cf.* Fig. 20c), suggesting that other mechanisms play a role here, such as the decrease of centre excitation.

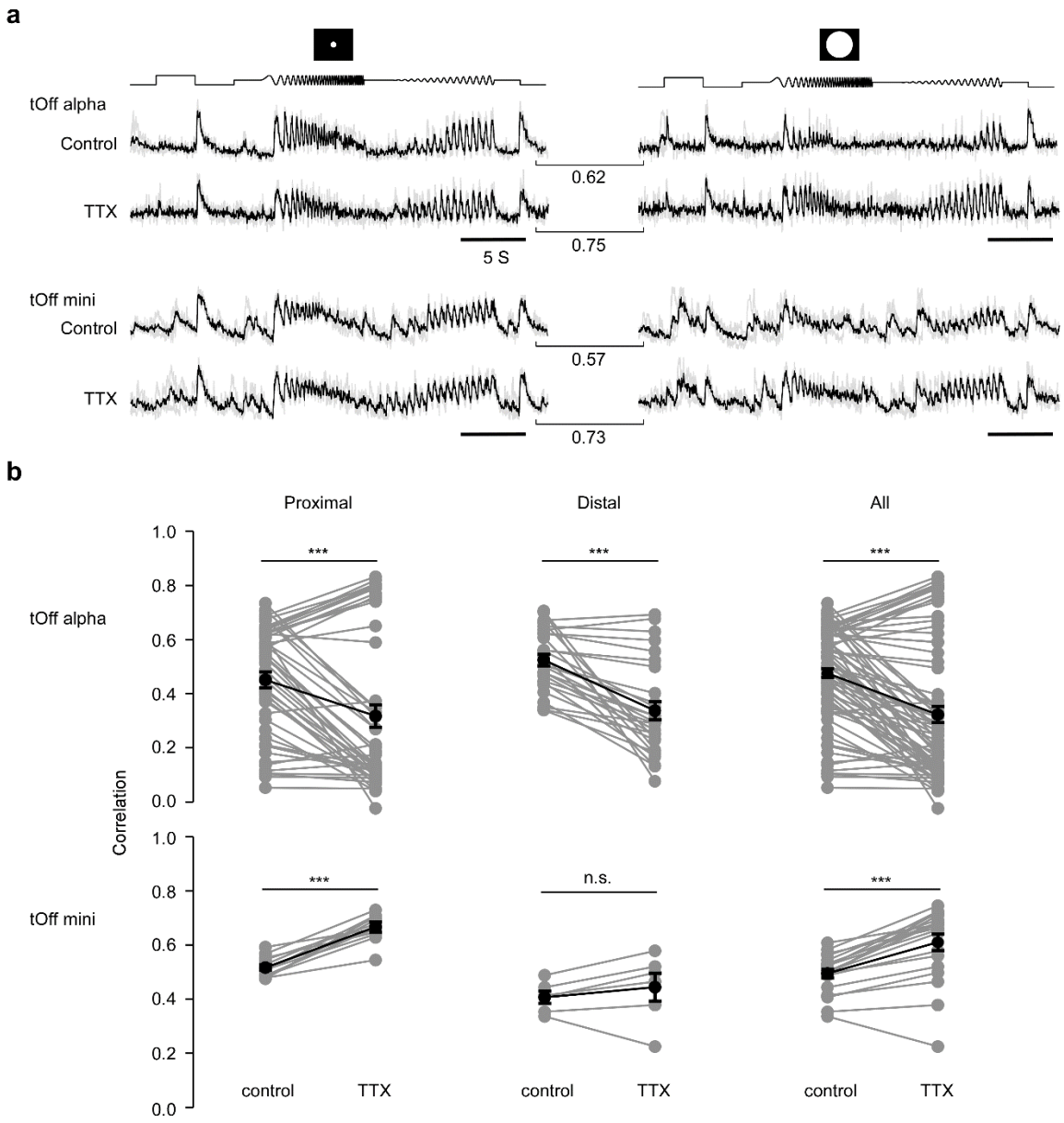

Figure 21 | Effects of local TTX application on chirp responses in tOff alpha and tOff mini cells.

a, Exemplary responses of one ROI from an tOff alpha and tOff mini cell to local and full-field chirp before and during TTX application. Values between the traces indicate linear correlation coefficient of the corresponding traces. **b,** Correlation of local and full-field chirp responses before and during TTX application as shown in (a). (n=5 tOff alpha cells, 21 proximal ROIs, 45 distal ROIs, 66 ROIs in total; n=3

tOff mini cells, 11 proximal ROIs, 17 distal ROIs, 28 ROIs in total). Statistics test same as (Fig. 19), alpha=0.05, *p<0.05, **p<0.01, ***p<0.001.

Together, my pharmacological data shows that local TTX application to the soma induces differential effects in tOff alpha and tOff mini cells. This results lend further support to the hypothesis that the different dendritic integration properties of the two cell types (partially) rely on different sets of voltage-gated channels. However, because TTX can also affect the retinal network upstream of the RGCs, further experiments – possibly with intracellular Na^+ channel blockers or genetically targeted modifications – are needed to further investigate the role of (somatic) sodium channels in RGC dendritic integration.

5 Discussion

In this thesis, I studied dendritic integration in four types of mouse Off RGCs – tOff alpha, tOff mini, sOff, and F-mini^{Off} – using recordings of local, light-evoked dendritic activity and compartmental modelling. Comparison of the four RGC types revealed two distinct spatial dendritic integration profiles: The first profile was observed in tOff alpha RGCs, where, as the distance from the soma increased, the RF area decreased and dendritic RFs became increasingly non-overlapping, with a minimal offset between recording site and respective RF centre. The second profile was observed in tOff mini and sOff RGCs, where RFs overlapped extensively and changed little in area, with their centres systematically shifted towards the soma. F-mini^{Off} cells can be considered to belong to the second category as well – with some particularities related to the high asymmetry of their dendritic arbour. In addition, dendritic segments in the different cell types displayed a notable difference in temporal signal correlation, with tOff alpha cells exhibiting the lowest and tOff mini cells the highest correlations for local chirps. In addition, sOff cells displayed the largest difference in temporal correlation between local and full-field chirp, suggesting a strong contribution of inhibitory surround. A morphologically inspired biophysical model revealed that distinct combinations of morphology and ion channel densities are required to explain these experimentally observed dendritic integration profiles. Local application of TTX to the soma showed significant effects on RF size of proximal dendrites in tOff mini but not tOff alpha cells, confirming distinct roles of voltage-gated Na^+ channels in shaping dendritic integration in these two cell types.

5.1 The relevance of type-specific dendritic integration in RGCs for visual processing

One key finding of this thesis was that different RGCs show type-specific dendritic integration profiles. What could the distinct integration rules be good for in the cell's visual computations? In tOff alpha RGCs (Krieger et al., 2017; Pang et al., 2003; Van Wyk et al., 2009), as the distance from the soma increased, RF area decreased and dendritic RFs became increasingly non-overlapping, with a minimal offset between the recording site and the respective RF centre. In

addition, activity on different dendritic branches was only moderately correlated. The more isolated, independent dendritic segments in tOff alpha cells may help them to detect fine structures of visual stimuli. This is reminiscent of what has been reported about On alpha cells, which possess nonlinear RFs and respond to patterns that contain local structures finer than the cell's RF centre (Schwartz et al., 2012). In contrast, tOff mini cell dendrites show large, overlapping RFs that changed little across the dendritic arbour. In addition, temporal signals of all tOff mini dendrites are highly synchronized, suggesting that they may reliably detect stimuli, independent of their location within the RF. For sOff cells, the temporal correlation of different dendritic segments greatly decreased when increasing the light stimulus size, suggesting that its computational properties change for extended visual stimuli. F-mini^{Off} cells showed some similar integration properties to tOff mini and sOff cells with some particularities related to the high asymmetry of their dendritic arbour (Rousso et al., 2016). These considerations suggest that dendritic integration properties may have important relevance to type-specific selectivity for visual features.

5.2 Mechanisms supporting cell-type-specific dendritic integration

Previous theoretical studies have suggested that alpha RGCs – with their large dendritic arbours, thick and short proximal branches, but thin and long distal branches (Wässle et al., 1981) – feature independent dendritic segments (Koch et al., 1982). In contrast, RGCs with a constant dendritic diameter and branch length across their dendritic arbour, are thought to produce densely coupled dendritic segments. In these RGCs, their morphology could enable more efficient dendritic back propagation, and therefore lead to the synchronization of dendritic signals (reviewed in (Tran-Van-Minh et al., 2015)). Indeed, more independent dendritic segments in tOff alpha cells were observed, but more spatially synchronized dendritic segments in tOff mini, sOff and F-mini^{Off} cells. For tOff mini and tOff alpha cells, their forward and backward propagation were differentially modulated by the same combinations of ion channel densities, indicating that dendritic morphology is a key determinant of signal propagation efficiency. However, the simulation results suggest that the dendritic integration properties of tOff alpha and tOff mini RGCs could not be explained by dendritic morphology alone but

require dendritic ion channels as described previously (Maturana et al., 2014; van Rossum et al., 2003).

5.3 Do local circuit properties contribute to type-specific dendritic integration?

The four types of Off RGCs studied here make connections with partially different sets of presynaptic BCs due to their different dendritic stratification depth: tOff alpha cells predominantly contact to transient type 3a and 4 BCs, while sOff cells mainly form excitatory synapses with the more sustained type 1 and 2 BCs (Bae et al., 2018; Helmstaedter et al., 2013; Yu et al., 2018). As tOff mini and tOff alpha co-stratified in the IPL, they are likely to receive excitatory inputs from the same BC types. In line with this connectivity, most ROIs from tOff alpha and tOff mini cells exhibited more transient responses than those from sOff cells (Fig. 15), suggesting some of the input features (e.g. transient versus sustained) can be recorded in retinal ganglion cell dendrites. However, the response properties of RGC dendrites are not only shaped by excitatory inputs but also inhibitory inputs from ACs. They often provide surround inhibition, attenuating the excitatory inputs (Roska et al., 2006). Accordingly, the correlation of dendritic signals in response to full-field chirp was lower than that in response to local chirp. Besides the connected types of BCs and ACs, the input distribution of excitation and inhibition along dendrites can shape dendritic integration in RGCs, such as DSGCs (reviewed in (Mauss et al., 2017; Vaney et al., 2012)).

Although contributions of excitatory and inhibitory inputs to the type-specific dendritic integration cannot be excluded, the results present in this thesis suggest that the intrinsic properties play a key role. For example, despite the fact that the excitatory input profiles of tOff mini and sOff cells are different due to their dendrites stratifying in different IPL depths, they show similar spatial dendritic integration, with highly synchronized dendrites. This suggests that the different input profiles do not act as a main contributor to their spatial dendritic integration.

RGCs not only make chemical synaptic connections with BCs and ACs, they can also be connected to ACs and other RGCs via gap junctions (Schubert et al., 2005; Trenholm et al., 2014; Volgyi et al., 2005). It has been reported that Off alpha cells form gap junctions with three to

eight neighbouring RGCs (Volgyi et al., 2005). If the gap-junction between a tOff alpha and its neighbours contribute substantially to the dendritic integration, activity in the coupled RGCs may affect dendritic signalling. One result of this might be that especially in the distal dendrites, dendritic RFs "shift away" from the soma. Such an effect may have contributed to our observation that RFs of distal ROIs in tOff alpha cells were local. To test this, further experiments would be required. For example, pharmacologically blocking the gap junctions and measuring the impacts on the size and position of distal RFs. For the other three types, their distal RFs systematically shifted towards the soma, less likely to result from the gap junctions with other RGCs.

Taken together, chemical and electrical synapses may indeed contribute to dendritic integration in RGCs. Therefore, it would be important and interesting to explore these effects in future studies, such as using computational models that consider the distributions of synapses along the dendrites and how this affects dendritic integration.

5.4 Reliability of RGC classification in this study

Recent studies have classified RGCs into different types based on specific morphological, functional or genetic criteria. For example, the latest functional study clustered mouse RGCs into ~30 types based on their light response properties (Baden et al., 2016), while a recent anatomical study classified RGCs into 47 types (Bae et al., 2018), and single cell transcriptome analysis identified 40 RGC types (Rheaume et al., 2018). The differences in the total number of RGC types identified in these studies may have different explanations. For example, over-clustering RGCs based on their morphology, difficulties in distinguishing RGC types functionally based on a limited stimulus set, etc. Nevertheless, the number of RGC types in mouse appears to consolidate at 40+ types.

In this thesis, the recorded RGCs were grouped by hierarchical clustering with *k*-means (based on their morphological properties defined in Bae et al. (2018)). Why the clustering was very robust, it cannot be completely excluded that individual cells were misclassified. There are three possible causes. First, all the cell morphologies were acquired through two-photon

microscopy with a spatial resolution of 0.32-0.66 µm/pixel (x-y) and 0.8-1 µm/frame (z), while the distal dendrites can be thinner than 0.5 µm (*cf.* Fig. 18). Thus, the relatively low spatial resolution might induce biases while measuring the morphological parameters (and this was also the reason, why dendritic parameters from EM data were used for the model). Second, only four morphological criteria were used for clustering: soma size, dendritic arbour area, dendritic arbour stratification difference and asymmetry. In future studies, more morphological properties may be used to validate the rigidity of the clustering. Third, no clear criteria were used to stop the clustering. While the grouped cells were compared with the previously reported types, the lack of clear criteria may have induced the under- (or over-) clustering of the recorded RGCs. In future studies, it may be helpful to use additional criteria for clustering, such as functional properties and/or genetic markers.

6 Future directions

6.1 Towards a more realistic model to study mechanisms underlying dendritic integration

In this work, a simple 1D biophysical model was built to investigate the potential mechanisms underlying type-specific dendritic integration. The model was based on the morphological parameters extracted from an EM dataset (Bae et al., 2018), and was able to successfully reproduce important experimentally observed RGC dendritic integration properties by changing the densities of different ion channels. However, there are a number of factors that could be considered in a future extended version of the model.

First, it has been reported that the branching pattern is an important variable for determining the propagation efficiency of dendritic signals, mainly because of the diameter changes at branch-points (Ferrante et al., 2013). In this study, signal propagation was simulated in a 1D model, which acknowledged the tapering in dendrite diameter, but did not consider the 2D branching pattern. While the 1D model was able to capture the key properties for the modelled RGCs, it will be interesting to extend the model to a full 2D version. Second, density and complement of ion channels can vary along the dendrite (reviewed in (Hausser et al., 2000b; Van Hook et al., 2019)), raising the possibility that spatially varying ion channel densities would allow for more refined control over dendritic computations. Finally, dendritic signalling is driven by the complex interaction of excitatory and inhibitory inputs, thus more realistic modelling dendritic signals can be expected if the effect of spatial distribution of excitatory and inhibitory synapses in different RGC types are considered.

6.2 Studying dendritic calcium and voltage integration at the same time

While Ca^{2+} imaging is a well-established and robust method, it has also a number of disadvantages, including low temporal resolution compare to electrophysiology, background signals induced by the laser and non-linear relationship with the membrane potential changes. Most critically, since intracellular Ca^{2+} does not only reflect voltage-gated channel activity but is also modulated by other sources, such as ligand-gated channels (e.g. GluRs) and the

intracellular stores (e.g. endoplasmic reticulum (Rizzuto and Pozzan,2006)), the usefulness of Ca^{2+} as a proxy for changes in membrane potential needs to be carefully considered for every neuron type. For instance, in some cortical neurons, it has been reported that Ca^{2+} and voltage are differentially integrated in their dendrites (Roome and Kuhn, 2018; Tran-Van-Minh et al., 2016). For example, in cerebellar interneurons, Ca^{2+} is integrated in a linear or supra-linear manner, while the voltage is integrated sub-linearly (Tran-Van-Minh et al., 2016). Therefore, it would be important to study dendritic integration of voltage and Ca^{2+} in individual RGCs ideally simultaneously. However, it is challenging to directly study dendritic voltage signals electrophysiologically because it is difficult to record the dendritic membrane potentials from the thin dendrite by patch-clamp. Recently, the development of genetically encoded voltage indicators (GEVIs, e.g. (Chamberland et al., 2017; Knopfel et al., 2015; Lacroix and Bezanilla, 2012)) present a promising tool to investigate the membrane potential dynamics in dendrites. Thus, by combining GEVI-based two-photon voltage with Ca^{2+} imaging, the spatio-temporal computation of voltage and Ca^{2+} in dendrites can be studied.

6.3 Functional implications of specific dendritic integration in different RGC types

Another challenging aspect of this project was to understand the functional role of type-specific dendritic integration in visual processing. Our data revealed local dendritic integration in tOff alpha cells and global dendritic integration in tOff mini, sOff and F-mini^{Off} cells, but how this specific dendritic integration serves efficient processing of visual information in their circuits needs to be further studied. One possibility would be to extract the information coded by dendritic segments across the dendritic arbour in different RGC types under naturalistic stimulations.

When investigating the functional role of dendritic integration for visual processing, one needs to keep in mind that the mouse retina is not homogeneous. First, it has been shown that RGC types and their circuits may morphologically and likely also functionally vary across the retina (Bleckert et al., 2014; Röhlich et al., 1994; Warwick et al., 2018). For example, sustained On and Off alpha cells show a gradual change in their dendritic arbour size and cell density along the

nasal-temporal axis of the retina, with smaller arbours and higher cell density in the temporal retina (Bleckert et al., 2014). In addition, the tOff alpha studied here, have been reported to exhibit more transient light response in the ventral retina, while they tend to show more sustained light response in the dorsal retina (Warwick et al., 2018). These morphological and functional differences within the same cell types suggest that dendritic integration properties might vary across the retina even within the same type of cell.

Second, mice feature an opsin expression gradient along the dorso-ventral axis of the retina (Baden et al., 2013b; Haverkamp et al., 2005; Röhlich et al., 1994). As a result, under photopic conditions, RGCs in the dorsal retina are mainly driven by green-sensitive M-opsin, while RGCs in the ventral retina are mainly driven by UV-sensitive S-opsin. Surprisingly, recent data shows that RGCs in the dorsal retinal do not show colour-opponent responses, which is prominent in the ventral RGCs (Szatko et al., 2019). In addition, a behavioural study suggests that mice can discriminate colours only in their upper visual field (Denman et al., 2018). These findings support the notion that there are substantial differences in RGC circuits between the ventral and dorsal retina.

Thus, to understand the roles of dendritic integration in the visual processing of their circuits, future studies should not only characterize dendritic integration properties between cell types, but also the same types at different locations across the retina.

7 Outlook

In this study, dendritic calcium signals acquired through two-photon imaging from individual cells revealed that different types of RGCs exhibit highly diverse spatio-temporal dendritic integration profiles. Some RGC types featured compartmentalized, isolated dendritic signals, while others displayed strong signal synchronization across their entire dendritic arbour. Computational modelling suggests that morphology alone cannot explain these differences. Instead, specific combinations of dendritic morphology and ion channel densities are required.

However, how the type-specific dendritic integration relates to their specific visual processing and what the contributions of different morphologies, ion channel densities and synaptic inputs contribute to specific dendritic integration profiles remain to be investigated. The understanding and recordings of natural scenes from mouse perspective, the development of new biosensors for imaging excitatory and inhibitory inputs and dendritic voltage (e.g. (Chamberland et al., 2017; Marvin et al., 2013), see 6.2), together with more biophysically realistic models (see 6.1), are promising directions for addressing these questions.

Understanding the dendritic integration rules and the underlying mechanistic principles are crucial to understand how information received across the dendritic arbour is processed before the information is relayed to downstream processing neurons (see 6.3). This has also important implications for research on retinal diseases. For example, in cat glaucomatous retina, RGCs showed shorter dendritic length, less dendritic branches and smaller somata compared to those in the normal retina (Shou et al., 2003). How these morphological changes affect the cell's AP output and what the consequences for the neural computations can be predicted if the dendritic integration rules are better understood.

8 References

Abrahamsson, T., Cathala, L., Matsui, K., Shigemoto, R., and DiGregorio, D.A. (2012). Thin Dendrites of Cerebellar Interneurons Confer Sublinear Synaptic Integration and a Gradient of Short-Term Plasticity. Neuron *73*, 1159-1172.

Altimus, C.M., Guler, A.D., Alam, N.M., Arman, A.C., Prusky, G.T., Sampath, A.P., and Hattar, S. (2010). Rod photoreceptors drive circadian photoentrainment across a wide range of light intensities. Nat Neurosci *13*, 1107-1112.

Ames, A., and Nesbett, F.B. (1981). Invitro Retina as an Experimental-Model of the Central Nervous-System. J Neurochem *37*, 867-877.

Awatramani, G.B., and Slaughter, M.M. (2000). Origin of transient and sustained responses in ganglion cells of the retina. Journal of Neuroscience *20*, 7087-7095.

Baden, T., Berens, P., Bethge, M., and Euler, T. (2013a). Spikes in mammalian bipolar cells support temporal layering of the inner retina. Curr Biol *23*, 48-52.

Baden, T., Berens, P., Franke, K., Roman Roson, M., Bethge, M., and Euler, T. (2016). The functional diversity of retinal ganglion cells in the mouse. Nature *529*, 345-350.

Baden, T., Schubert, T., Berens, P., and Euler, T. (2018). The Functional Organization of Vertebrate Retinal Circuits for Vision. *Oxford Research Encyclopedia of Neuroscience*, 10.1093/acrefore/9780190264086.9780190264013.9780190264068.

Baden, T., Schubert, T., Chang, L., Wei, T., Zaichuk, M., Wissinger, B., and Euler, T. (2013b). A tale of two retinal domains: near-optimal sampling of achromatic contrasts in natural scenes through asymmetric photoreceptor distribution. Neuron *80*, 1206-1217.

Bae, J.A., Mu, S., Kim, J.S., Turner, N.L., Tartavull, I., Kemnitz, N., Jordan, C.S., Norton, A.D., Silversmith, W.M., Prentki, R*., et al.* (2018). Digital Museum of Retinal Ganglion Cells with Dense Anatomy and Physiology. Cell *173*, 1293-1306 e1219.

Bean, B.P. (2007). The action potential in mammalian central neurons. Nature Reviews Neuroscience *8*, 451-465.

Behabadi, B.F., and Mel, B.W. (2014). Mechanisms underlying subunit independence in pyramidal neuron dendrites. Proc Natl Acad Sci U S A *111*, 498-503.

Behrens, C., Schubert, T., Haverkamp, S., Euler, T., and Berens, P. (2016). Connectivity map of bipolar cells and photoreceptors in the mouse retina. Elife *5*.

Behrens, C., Zhang, Y., Yadav, S.C., Haverkamp, S., Irsen, S., Korympidou, M.M., Schaedler, A., Dedek, K., Smith, R.G., Euler, T.*, et al.* (2019). Retinal horizontal cells use different synaptic sites for global feedforward and local feedback signaling BioRxiv, 10.1101/780031.

Bernander, O., Douglas, R.J., Martin, K.A., and Koch, C. (1991). Synaptic background activity influences spatiotemporal integration in single pyramidal cells. Proc Natl Acad Sci U S A *88*, 11569-11573.

Bikson, M., Ghai, R.S., Baraban, S.C., and Durand, D.M. (1999). Modulation of burst frequency, duration, and amplitude in the zero-Ca2+ model of epileptiform activity. Journal of Neurophysiology *82*, 2262-2270.

Bleckert, A., Schwartz, G.W., Turner, M.H., Rieke, F., and Wong, R.O.L. (2014). Visual Space Is Represented by Nonmatching Topographies of Distinct Mouse Retinal Ganglion Cell Types. Curr Biol *24*, 310-315.

Bloomfield, S.A. (1996). Effect of spike blockade on the receptive-field size of amacrine and ganglion cells in the rabbit retina. Journal of Neurophysiology *75*, 1878-1893.

Borg-Graham, L.J. (2001). The computation of directional selectivity in the retina occurs presynaptic to the ganglion cell. Nature Neuroscience *4*, 176-183.

Branco, T., and Hausser, M. (2010). The single dendritic branch as a fundamental functional unit in the nervous system. Curr Opin Neurobiol *20*, 494-502.

Brandstatter, J.H., and Hack, I. (2001). Localization of glutamate receptors at a complex synapse - The mammalian photoreceptor synapse. Cell Tissue Res *303*, 1-14.

Breuninger, T., Puller, C., Haverkamp, S., and Euler, T. (2011). Chromatic Bipolar Cell Pathways in the Mouse Retina. Journal of Neuroscience *31*, 6504-6517.

Carnevale, N.T., and and Hines, M.L. (2006). The NEURON Book (Cambridge, UK: Cambridge University Press).

Chamberland, S., Yang, H.H., Pan, M.M., Evans, S.W., Guan, S.H., Chavarha, M., Yang, Y., Salesse, C., Wu, H.D., Wu, J.C*., et al.* (2017). Fast two-photon imaging of subcellular voltage dynamics in neuronal tissue with genetically encoded indicators. Elife *6*.

Chapot, C.A., Behrens, C., Rogerson, L.E., Baden, T., Pop, S., Berens, P., Euler, T., and Schubert, T. (2017). Local Signals in Mouse Horizontal Cell Dendrites. Curr Biol *27*, 3603-3615 e3605.

Cichon, J., and Gan, W.B. (2015). Branch-specific dendritic Ca2+ spikes cause persistent synaptic plasticity. Nature *520*, 180-U180.

Connelly, W.M., and Stuart, G.J. (2019). Local versus Global Dendritic Integration. Neuron *103*, 173-174.

Cui, J.J., and Pan, Z.H. (2008). Two types of cone bipolar cells express voltage-gated Na+ channels in the rat retina. Visual Neurosci *25*, 635-645.

Denman, D.J., Luviano, J.A., Ollerenshaw, D.R., Cross, S., Williams, D., Buice, M.A., Olsen, S.R., and Reid, R.C. (2018). Mouse color and wavelength-specific luminance contrast sensitivity are non-uniform across visual space. Elife *7*.

Deny, S., Ferrari, U., Mace, E., Yger, P., Caplette, R., Picaud, S., Tkacik, G., and Marre, O. (2017). Multiplexed computations in retinal ganglion cells of a single type. Nat Commun *8*, 1964.

DeVries, S.H. (2000). Bipolar cells use kainate and AMPA receptors to filter visual information into separate channels. Neuron *28*, 847-856.

Diamond, J.S. (2017). Inhibitory Interneurons in the Retina: Types, Circuitry, and Function. Annu Rev Vis Sci *3*, 1-24.

Ding, H., Smith, R.G., Poleg-Polsky, A., Diamond, J.S., and Briggman, K.L. (2016). Species-specific wiring for direction selectivity in the mammalian retina. Nature *535*, 105-110.

Dmitriev, A.V., Gavrikov, K.E., and Mangel, S.C. (2012). GABA-mediated spatial and temporal asymmetries that contribute to the directionally selective light responses of starburst amacrine cells in retina. J Physiol-London *590*, 1699-1720.

Dorostkar, M.M., Dreosti, E., Odermatt, B., and Lagnado, L. (2010). Computational processing of optical measurements of neuronal and synaptic activity in networks. J Neurosci Meth *188*, 141-150.

Eggers, E.D., and Lukasiewicz, P.D. (2006). GABAA, GABAC and glycine receptor-mediated inhibition differentially affects light-evoked signalling from mouse retinal rod bipolar cells. The Journal of Physiology *572*, 215-225.

Euler, T., and Denk, W. (2001). Dendritic processing. Curr Opin Neurobiol *11*, 415-422.

Euler, T., Detwiler, P.B., and Denk, W. (2002). Directionally selective calcium signals in dendrites of starburst amacrine cells. Nature *418*, 845-852.

Euler, T., Hausselt, S.E., Margolis, D.J., Breuninger, T., Castell, X., Detwiler, P.B., and Denk, W. (2009). Eyecup scope-optical recordings of light stimulus-evoked fluorescence signals in the retina. Pflug Arch Eur J Phy *457*, 1393-1414.

Euler, T., Schneider, H., and Wassle, H. (1996). Glutamate responses of bipolar cells in a slice preparation of the rat retina. Journal of Neuroscience *16*, 2934-2944.

Ferrante, M., Migliore, M., and Ascoli, G.A. (2013). Functional impact of dendritic branch-point morphology. J Neurosci *33*, 2156-2165.

Finch, E.A., and Augustine, G.J. (1998). Local calcium signalling by inositol-1,4,5-trisphosphate in Purkinje cell dendrites. Nature *396*, 753-756.

Fohlmeister, J.F., and Miller, R.F. (1997). Impulse encoding mechanisms of ganglion cells in the tiger salamander retina. J Neurophysiol *78*, 1935-1947.

Franke, K., and Baden, T. (2017). General features of inhibition in the inner retina. J Physiol-London *595*, 5507-5515.

Franke, K., Berens, P., Schubert, T., Bethge, M., Euler, T., and Baden, T. (2017). Inhibition decorrelates visual feature representations in the inner retina. Nature *542*, 439-444.

Franke, K., Chagas, A.M., Zhao, Z.J., Zimmermann, M.J.Y., Bartel, P., Qiu, Y.R., Szatko, K.P., Baden, T., and Euler, T. (2019). An arbitrary-spectrum spatial visual stimulator for vision research. Elife *8*.

Fransen, J.W., and Borghuis, B.G. (2017). Temporally Diverse Excitation Generates Direction-Selective Responses in ON- and OFF-Type Retinal Starburst Amacrine Cells. Cell Reports *18*, 1356-1365.

Gavrikov, K.E., Nilson, J.E., Dmitriev, A.V., Zucker, C.L., and Mangel, S.C. (2006). Dendritic compartmentalization of chloride cotransporters underlies directional responses of starburst amacrine cells in retina. Proc Natl Acad Sci U S A *103*, 18793-18798.

Goldstein, S.S., and Rall, W. (1974). Changes of action potential shape and velocity for changing core conductor geometry. Biophys J *14*, 731-757.

Grassmeyer, J.J., and Thoreson, W.B. (2017). Synaptic Ribbon Active Zones in Cone Photoreceptors Operate Independently from One Another. Frontiers in Cellular Neuroscience *11*.

Grimes, W.N., Zhang, J., Graydon, C.W., Kachar, B., and Diamond, J.S. (2010). Retinal parallel processors: more than 100 independent microcircuits operate within a single interneuron. Neuron *65*, 873-885.

Grunert, U., and Wassle, H. (1993). Immunocytochemical Localization of Glycine Receptors in the Mammalian Retina. J Comp Neurol *335*, 523-537.

Gulledge, A.T., Kampa, B.M., and Stuart, G.J. (2005). Synaptic integration in dendritic trees. Journal of Neurobiology *64*, 75-90.

Guo, T., Tsai, D., Bai, S., Morley, J.W., Suaning, G.J., Lovell, N.H., and Dokos, S. (2014). Understanding the retina: a review of computational models of the retina from the single cell to the network level. Crit Rev Biomed Eng *42*, 419-436.

Hausser, M., Spruston, N., and Stuart, G.J. (2000a). Diversity and dynamics of dendritic signaling. Science *290*, 739-744.

Hausser, M., Spruston, N., and Stuart, G.J. (2000b). Diversity and dynamics of dendritic signaling. Science *290*, 739-744.

Haverkamp, S., Wassle, H., Duebel, J., Kuner, T., Augustine, G.J., Feng, G.P., and Euler, T. (2005). The primordial, blue-cone color system of the mouse retina. Journal of Neuroscience *25*, 5438-5445.

Helmstaedter, M., Briggman, K.L., Turaga, S.C., Jain, V., Seung, H.S., and Denk, W. (2013). Connectomic reconstruction of the inner plexiform layer in the mouse retina. Nature *500*, 168-174.

Hines, M.L., and Carnevale, N.T. (1997). The NEURON simulation environment. Neural Comput *9*, 1179-1209.

Hoffman, D.A., Magee, J.C., Colbert, C.M., and Johnston, D. (1997). K+ channel regulation of signal propagation in dendrites of hippocampal pyramidal neurons. Nature *387*, 869-875.

Huguenard, J.R., Hamill, O.P., and Prince, D.A. (1989). Sodium channels in dendrites of rat cortical pyramidal neurons. Proc Natl Acad Sci U S A *86*, 2473-2477.

Iacaruso, M.F., Gasler, I.T., and Hofer, S.B. (2017). Synaptic organization of visual space in primary visual cortex. Nature *547*, 449-452.

Jaffe, D.B., and Carnevale, N.T. (1999). Passive normalization of synaptic integration influenced by dendritic architecture. Journal of Neurophysiology *82*, 3268-3285.

Jia, H.B., Varga, Z., Sakmann, B., and Konnerth, A. (2014). Linear integration of spine Ca2+ signals in layer 4 cortical neurons in vivo. Proc Natl Acad Sci U S A *111*, 9277-9282.

Kampa, B.M., Letzkus, J.J., and Stuart, G.J. (2007). Dendritic mechanisms controlling spike-timing-dependent synaptic plasticity. Trends in Neurosciences *30*, 456-463.

Kaneko, Y., and Watanabe, S.-I. (2007). Expression of Nav1.1 in rat retinal AII amacrine cells. Neuroscience Letters *424*, 83-88.

Katz, Y., Menon, V., Nicholson, D.A., Geinisman, Y., Kath, W.L., and Spruston, N. (2009). Synapse Distribution Suggests a Two-Stage Model of Dendritic Integration in CA1 Pyramidal Neurons. Neuron *63*, 171-177.

Kemmler, R., Schultz, K., Dedek, K., Euler, T., and Schubert, T. (2014). Differential Regulation of Cone Calcium Signals by Different Horizontal Cell Feedback Mechanisms in the Mouse Retina. Journal of Neuroscience *34*, 11826-11843.

Kerlin, A., Boaz, M., Flickinger, D., MacLennan, B.J., Dean, M.B., Davis, C., Spruston, N., and Svoboda, K. (2019). Functional clustering of dendritic activity during decision-making. Elife *8*.

Kim, J.S., Greene, M.J., Zlateski, A., Lee, K., Richardson, M., Turaga, S.C., Purcaro, M., Balkam, M., Robinson, A., Behabadi, B.F.*, et al.* (2014). Space-time wiring specificity supports direction selectivity in the retina. Nature *509*, 331-+.

Kitamura, K., and Kano, M. (2013). Dendritic calcium signaling in cerebellar Purkinje cell. Neural Netw *47*, 11-17.

Knopfel, T., Gallero-Salas, Y., and Song, C.C. (2015). Genetically encoded voltage indicators for large scale cortical imaging come of age. Curr Opin Chem Biol *27*, 75-83.

Koch, C., Poggio, T., and Torre, V. (1982). Retinal ganglion cells: a functional interpretation of dendritic morphology. Philos Trans R Soc Lond B Biol Sci *298*, 227-263.

Koike, C., Obara, T., Uriu, Y., Numata, T., Sanuki, R., Miyata, K., Koyasu, T., Ueno, S., Funabiki, K., Tani, A.*, et al.* (2010). TRPM1 is a component of the retinal ON bipolar cell transduction channel in the mGluR6 cascade. Proc Natl Acad Sci U S A *107*, 332-337.

Koren, D., Grove, J.C.R., and Wei, W. (2017). Cross-compartmental Modulation of Dendritic Signals for Retinal Direction Selectivity. Neuron *95*, 914-927 e914.

Korenbrot, J.I. (2012). Speed, sensitivity, and stability of the light response in rod and cone photoreceptors: Facts and models. Progress in Retinal and Eye Research *31*, 442-466.

Krieger, B., Qiao, M., Rousso, D.L., Sanes, J.R., and Meister, M. (2017). Four alpha ganglion cell types in mouse retina: Function, structure, and molecular signatures. PLoS One *12*, e0180091.

Lacroix, J.J., and Bezanilla, F. (2012). Tuning the Voltage-Sensor Motion with a Single Residue. Biophys J *103*, L23-L25.

Lai, H.C., and Jan, L.Y. (2006). The distribution and targeting of neuronal voltage-gated ion channels. Nat Rev Neurosci *7*, 548-562.

Lall, G.S., Revell, V.L., Momiji, H., Al Enezi, J., Altimus, C.M., Guler, A.D., Aguilar, C., Cameron, M.A., Allender, S., Hankins, M.W.*, et al.* (2010). Distinct Contributions of Rod, Cone, and Melanopsin Photoreceptors to Encoding Irradiance. Neuron *66*, 417-428.

Larkum, M.E., Nevian, T., Sandler, M., Polsky, A., and Schiller, J. (2009). Synaptic integration in tuft dendrites of layer 5 pyramidal neurons: a new unifying principle. Science *325*, 756-760.

Lee, S., Zhang, Y., Chen, M.G., and Zhou, Z.J. (2016). Segregated Glycine-Glutamate Co-transmission from vGluT3 Amacrine Cells to Contrast-Suppressed and Contrast-Enhanced Retinal Circuits. Neuron *90*, 27-34.

Lee, S., and Zhou, Z.J. (2006). The synaptic mechanism of direction selectivity in distal processes of starburst amacrine cells. Neuron *51*, 787-799.

Li, W., and DeVries, S.H. (2006). Bipolar cell pathways for color and luminance vision in a dichromatic mammalian retina. Nature Neuroscience *9*, 669-675.

Liu, X., Hirano, A.A., Sun, X., Brecha, N.C., and Barnes, S. (2013). Calcium channels in rat horizontal cells regulate feedback inhibition of photoreceptors through an unconventional GABA- and pH-sensitive mechanism. The Journal of Physiology *591*, 3309-3324.

London, M., and Hausser, M. (2005). Dendritic computation. Annu Rev Neurosci *28*, 503-532.

Longair, M.H., Baker, D.A., and Armstrong, J.D. (2011). Simple Neurite Tracer: open source software for reconstruction, visualization and analysis of neuronal processes. Bioinformatics *27*, 2453-2454.

Losonczy, A., and Magee, J.C. (2006). Integrative properties of radial oblique Dendrites in hippocampal CA1 pyramidal neurons. Neuron *50*, 291-307.

Magee, J.C. (2000). Dendritic integration of excitatory synaptic input. Nat Rev Neurosci *1*, 181-190.

Major, G., Larkum, M.E., and Schiller, J. (2013). Active Properties of Neocortical Pyramidal Neuron Dendrites. Annual Review of Neuroscience, Vol 36 *36*, 1-+.

Manita, S., Miyakawa, H., Kitamura, K., and Murayama, M. (2017). Dendritic Spikes in Sensory Perception. Frontiers in Cellular Neuroscience *11*.

Margolis, D.J., Gartland, A.J., Euler, T., and Detwiler, P.B. (2010). Dendritic calcium signaling in ON and OFF mouse retinal ganglion cells. J Neurosci *30*, 7127-7138.

Marvin, J.S., Borghuis, B.G., Tian, L., Cichon, J., Harnett, M.T., Akerboom, J., Gordus, A., Renninger, S.L., Chen, T.W., Bargmann, C.I.*, et al.* (2013). An optimized fluorescent probe for visualizing glutamate neurotransmission. Nat Methods *10*, 162-170.

Masland, R.H. (2005). The many roles of starburst amacrine cells. Trends Neurosci *28*, 395-396.

Masland, R.H. (2012). The Neuronal Organization of the Retina. Neuron *76*, 266-280.

Masu, M., Iwakabe, H., Tagawa, Y., Miyoshi, T., Yamashita, M., Fukuda, Y., Sasaki, H., Hiroi, K., Nakamura, Y., Shigemoto, R.*, et al.* (1995). Specific Deficit of the on Response in Visual Transmission by Targeted Disruption of the Mglur6 Gene. Cell *80*, 757-765.

Maturana, M.I., Kameneva, T., Burkitt, A.N., Meffin, H., and Grayden, D.B. (2014). The effect of morphology upon electrophysiological responses of retinal ganglion cells: simulation results. J Comput Neurosci *36*, 157-175.

Mauss, A.S., Vlasits, A., Borst, A., and Feller, M. (2017). Visual Circuits for Direction Selectivity. Annu Rev Neurosci *40*, 211-230.

Milojkovic, B.A., Wuskell, J.P., Loew, L.M., and Antic, S.D. (2005). Initiation of sodium spikelets in basal dendrites of neocortical pyramidal neurons. J Membrane Biol *208*, 155-169.

Münch, T.A., and Werblin, F.S. (2006). Symmetric interactions within a homogeneous starburst cell network can lead to robust asymmetries in dendrites of starburst amacrine cells. Journal of Neurophysiology *96*, 471-477.

Murphy-Baum, B.L., and Taylor, W.R. (2018). Diverse inhibitory and excitatory mechanisms shape temporal tuning in transient OFF ganglion cells in the rabbit retina. J Physiol-London *596*, 477-495.

Nevian, T., Larkum, M.E., Polsky, A., and Schiller, J. (2007). Properties of basal dendrites of layer 5 pyramidal neurons: a direct patch-clamp recording study. Nature Neuroscience *10*, 206-214.

Nikonov, S.S., Kholodenko, R., Lem, J., and Pugh, E.N., Jr. (2006). Physiological features of the S- and M-cone photoreceptors of wild-type mice from single-cell recordings. J Gen Physiol *127*, 359-374.

O'Brien, B.J., Caldwell, J.H., Ehring, G.R., Bumsted O'Brien, K.M., Luo, S., and Levinson, S.R. (2008). Tetrodotoxin-resistant voltage-gated sodium channels Nav1.8 and Nav1.9 are expressed in the retina. J Comp Neurol *508*, 940-951.

Oesch, N., Euler, T., and Taylor, W.R. (2005). Direction-selective dendritic action potentials in rabbit retina. Neuron *47*, 739-750.

Ofer, N., Shefi, O., and Yaari, G. (2017). Branching morphology determines signal propagation dynamics in neurons. Scientific Reports *7*, 8877.

Ouzounov, D.G., Wang, T.Y., Wang, M.R., Feng, D.D., Horton, N.G., Cruz-Hernandez, J.C., Cheng, Y.T., Reimer, J., Tolias, A.S., Nishimura, N.*, et al.* (2017). In vivo three-photon imaging of activity of GCaMP6-labeled neurons deep in intact mouse brain. Nature Methods *14*, 388-+.

Pang, J.J., Gao, F., and Wu, S.M. (2003). Light-evoked excitatory and inhibitory synaptic inputs to ON and OFF alpha ganglion cells in the mouse retina. Journal of Neuroscience *23*, 6063-6073.

Pedregosa, F., Varoquaux, G., Gramfort, A., Michel, V., Thirion, B., Grisel, O., Blondel, M., Prettenhofer, P., Weiss, R., Dubourg, V.*, et al.* (2011). Scikit-learn: Machine Learning in Python. J Mach Learn Res *12*, 2825-2830.

Poirazi, P., Brannon, T., and Mel, B.W. (2003). Pyramidal neuron as two-layer neural network. Neuron *37*, 989-999.

Poleg-Polsky, A., Ding, H., and Diamond, J.S. (2018). Functional Compartmentalization within Starburst Amacrine Cell Dendrites in the Retina. Cell Rep *22*, 2898-2908.

Polsky, A., Mel, B., and Schiller, J. (2009). Encoding and Decoding Bursts by NMDA Spikes in Basal Dendrites of Layer 5 Pyramidal Neurons. Journal of Neuroscience *29*, 11891-11903.

Polsky, A., Mel, B.W., and Schiller, J. (2004). Computational subunits in thin dendrites of pyramidal cells. Nat Neurosci *7*, 621-627.

Pourcho, R.G. (1982). Dopaminergic Amacrine Cells in the Cat Retina. Brain Res *252*, 101-109.

Protti, D.A., Di Marco, S., Huang, J.Y., Vonhoff, C.R., Nguyen, V., and Solomon, S.G. (2014). Inner retinal inhibition shapes the receptive field of retinal ganglion cells in primate. J Physiol-London *592*, 49-65.

Puopolo, M., Hochstetler, S.E., Gustincich, S., Wightman, R.M., and Raviola, E. (2001). Extrasynaptic release of dopamine in a retinal neuron: Activity dependence and transmitter modulation. Neuron *30*, 211-225.

Rall, W., and Rinzel, J. (1973). Branch Input Resistance and Steady Attenuation for Input to One Branch of a Dendritic Neuron Model. Biophys J *13*, 648-688.

Regehr, W., Kehoe, J.S., Ascher, P., and Armstrong, C. (1993). Synaptically triggered action potentials in dendrites. Neuron *11*, 145-151.

Rheaume, B.A., Jereen, A., Bolisetty, M., Sajid, M.S., Yang, Y., Renna, K., Sun, L., Robson, P., and Trakhtenberg, E.F. (2018). Single cell transcriptome profiling of retinal ganglion cells identifies cellular subtypes. Nat Commun *9*, 2759.

Riggs, L.A., and Whittle, P. (1967). Human Occipital and Retinal Potentials Evoked by Subjectively Faded Visual Stimuli. Vision Res *7*, 441-&.

Rinzel, J., and Rall, W. (1974). Transient-Response in a Dendritic Neuron Model for Current Injected at One Branch. Biophys J *14*, 759-790.

Röhlich, P., van Veen, T., and Szél, Á. (1994). Two different visual pigments in one retinal cone cell. Neuron *13*, 1159-1166.

Roome, C.J., and Kuhn, B. (2018). Simultaneous dendritic voltage and calcium imaging and somatic recording from Purkinje neurons in awake mice. Nature Communications *9*.

Roorda, A., and Williams, D.R. (1999). The arrangement of the three cone classes in the living human eye. Nature *397*, 520-522.

Roska, B., Molnar, A., and Werblin, F.S. (2006). Parallel processing in retinal ganglion cells: How integration of space-time patterns of excitation and inhibition form the spiking output. Journal of Neurophysiology *95*, 3810-3822.

Roska, B., and Werblin, F. (2001). Vertical interactions across ten parallel, stacked representations in the mammalian retina. Nature *410*, 583-587.

Rousso, D.L., Qiao, M., Kagan, R.D., Yamagata, M., Palmiter, R.D., and Sanes, J.R. (2016). Two Pairs of ON and OFF Retinal Ganglion Cells Are Defined by Intersectional Patterns of Transcription Factor Expression. Cell Rep *15*, 1930-1944.

Sahani, M., and Linden, J.F. (2003). Evidence Optimization Techniques for Estimating Stimulus-Response Functions. Advances in neural information processing systems, 317-324.

Sanes, J.R., and Masland, R.H. (2015). The types of retinal ganglion cells: current status and implications for neuronal classification. Annu Rev Neurosci *38*, 221-246.

Sassoepognetto, M., Wassle, H., and Grunert, U. (1994). Glycinergic Synapses in the Rod Pathway of the Rat Retina - Cone Bipolar Cells Express the Alpha-1 Subunit of the Glycine Receptor. Journal of Neuroscience *14*, 5131-5146.

Schachter, M.J., Oesch, N., Smith, R.G., and Taylor, W.R. (2010). Dendritic spikes amplify the synaptic signal to enhance detection of motion in a simulation of the direction-selective ganglion cell. PLoS Comput Biol *6(8)*, e1000899. doi:1000810.1001371/journal.pcbi.1000899.

Schneeweis, D.M., and Schnapf, J.L. (1995). Photovoltage of rods and cones in the macaque retina. Science *268*, 1053-1056.

Schubert, T., Maxeiner, S., Krüger, O., Willecke, K., and Weiler, R. (2005). Connexin45 mediates gap junctional coupling of bistratified ganglion cells in the mouse retina. J Comp Neurol *490*, 29-39.

Schwartz, G.W., Okawa, H., Dunn, F.A., Morgan, J.L., Kerschensteiner, D., Wong, R.O., and Rieke, F. (2012). The spatial structure of a nonlinear receptive field. Nat Neurosci *15*, 1572-1580.

Shields, C.R., Tran, M.N., Wong, R.O.L., and Lukasiewicz, P.D. (2000). Distinct ionotropic GABA receptors mediate presynaptic and postsynaptic inhibition in retinal bipolar cells. Journal of Neuroscience *20*, 2673-2682.

Shou, T., Liu, J., Wang, W., Zhou, Y., and Zhao, K. (2003). Differential dendritic shrinkage of alpha and beta retinal ganglion cells in cats with chronic glaucoma. Invest Ophthalmol Vis Sci *44*, 3005-3010.

Sivyer, B., and Williams, S.R. (2013). Direction selectivity is computed by active dendritic integration in retinal ganglion cells. Nat Neurosci *16*, 1848-1856.

Spruston, N. (2008). Pyramidal neurons: dendritic structure and synaptic integration. Nature Reviews Neuroscience *9*, 206-221.

Spruston, N., Stuart, G., and Häusser, M. (2016). Principles of dendritic integration. In Dendrites, N. Spruston, G. Stuart, and M. Häusser, eds. (Oxford University Press).

Stuart, G., and Hausser, M. (1994). Initiation and Spread of Sodium Action-Potentials in Cerebellar Purkinje-Cells. Neuron *13*, 703-712.

Stuart, G.J., and Sakmann, B. (1994). Active Propagation of Somatic Action-Potentials into Neocortical Pyramidal Cell Dendrites. Nature *367*, 69-72.

Stuart, G.J., and Spruston, N. (2015). Dendritic integration: 60 years of progress. Nat Neurosci *18*, 1713-1721.

Sun, W., Matthews, E.A., Nicolas, V., Schoch, S., and Dietrich, D. (2016). NG2 glial cells integrate synaptic input in global and dendritic calcium signals. Elife *5*.

Szatko, K.P., Korympidou, M.M., Ran, Y., Berens, P., Dalkara, D., Schubert, T., Euler, T., and Franke, K. (2019). Neural circuits in the mouse retina support color vision in the upper visual field bioRxiv, 10.1101/745539.

Szél, Á., Röhlich, P., Gaffé, A.R., Juliusson, B., Aguirre, G., and Van Veen, T. (1992). Unique topographic separation of two spectral classes of cones in the mouse retina. J Comp Neurol *325*, 327-342.

Takahashi, H., and Magee, J.C. (2009). Pathway Interactions and Synaptic Plasticity in the Dendritic Tuft Regions of CA1 Pyramidal Neurons. Neuron *62*, 102-111.

Taylor, W.R. (1999). TTX attenuates surround inhibition in rabbit retinal ganglion cells. Visual Neurosci *16*, 285-290.

Theer, P., and Denk, W. (2006). On the fundamental imaging-depth limit in two-photon microscopy. J Opt Soc Am A *23*, 3139-3149.

Tran-Van-Minh, A., Abrahamsson, T., Cathala, L., and DiGregorio, D.A. (2016). Differential Dendritic Integration of Synaptic Potentials and Calcium in Cerebellar Interneurons. Neuron *91*, 837-850.

Tran-Van-Minh, A., Caze, R.D., Abrahamsson, T., Cathala, L., Gutkin, B.S., and DiGregorio, D.A. (2015). Contribution of sublinear and supralinear dendritic integration to neuronal computations. Front Cell Neurosci *9*, 67.

Trenholm, S., Johnson, K., Li, X., Smith, R.G., and Awatramani, G.B. (2011). Parallel Mechanisms Encode Direction in the Retina. Neuron *71*, 683-694.

Trenholm, S., McLaughlin, A.J., Schwab, D.J., Turner, M.H., Smith, R.G., Rieke, F., and Awatramani, G.B. (2014). Nonlinear dendritic integration of electrical and chemical synaptic inputs drives fine-scale correlations. Nat Neurosci *17*, 1759-1766.

van der Walt, S., Schonberger, J.L., Nunez-Iglesias, J., Boulogne, F., Warner, J.D., Yager, N., Gouillart, E., Yu, T., and Contributors, S.I. (2014). scikit-image: image processing in Python. Peerj *2*.

Van Hook, M.J., Nawy, S., and Thoreson, W.B. (2019). Voltage- and calcium-gated ion channels of neurons in the vertebrate retina. Progress in Retinal and Eye Research, 10.1016/j.preteyeres.2019.1005.1001.

van Rij, J., Wieling, M., Baayen, R., and van Rijn, H. (2017). itsadug: Interpreting Time Series and Autocorrelated Data Using GAMMs. R package version 2.3.

van Rossum, M.C., O'Brien, B.J., and Smith, R.G. (2003). Effects of noise on the spike timing precision of retinal ganglion cells. J Neurophysiol *89*, 2406-2419.

Van Wart, A., Boiko, T., Trimmer, J.S., and Matthews, G. (2005). Novel clustering of sodium channel Nav1.1 with ankyrin-G and neurofascin at discrete sites in the inner plexiform layer of the retina. Molecular and Cellular Neuroscience *28*, 661-673.

Van Wyk, M., Wassle, H., and Taylor, W.R. (2009). Receptive field properties of ON- and OFF-ganglion cells in the mouse retina. Visual Neurosci *26*, 297-308.

Vaney, D.I. (1984). Coronate Amacrine Cells in the Rabbit Retina Have the Starburst Dendritic Morphology. Proc R Soc Ser B-Bio *220*, 501-508.

Vaney, D.I., Sivyer, B., and Taylor, W.R. (2012). Direction selectivity in the retina: symmetry and asymmetry in structure and function. Nature Reviews Neuroscience *13*, 194-208.

Velte, T.J., and Masland, R.H. (1999). Action potentials in the dendrites of retinal ganglion cells. J Neurophysiol *81*, 1412-1417.

Velte, T.J., and Miller, R.F. (1995). Dendritic integration in ganglion cells of the mudpuppy retina. Vis Neurosci *12*, 165-175.

Vetter, P., Roth, A., and Hausser, M. (2001). Propagation of action potentials in dendrites depends on dendritic morphology. Journal of Neurophysiology *85*, 926-937.

Vielma, A.H., Retamal, M.A., and Schmachtenberg, O. (2012). Nitric oxide signaling in the retina: what have we learned in two decades? Brain Res *1430*, 112-125.

Vlasits, A.L., Morrie, R.D., Alexandra, T.V.M., Bleckert, A., Gainer, C.F., DiGregorio, D.A., and Feller, M.B. (2016). A Role for Synaptic Input Distribution in a Dendritic Computation of Motion Direction in the Retina. Neuron *89*, 1317-1330.

Voigt, T., and Wassle, H. (1987). Dopaminergic Innervation of a-Ii Amacrine Cells in Mammalian Retina. Journal of Neuroscience *7*, 4115-4128.

Volgyi, B., Abrams, J., Paul, D.L., and Bloomfield, S.A. (2005). Morphology and tracer coupling pattern of alpha ganglion cells in the mouse retina. J Comp Neurol *492*, 66-77.

Vroman, R., Klaassen, L.J., and Kamermans, M. (2013). Ephaptic communication in the vertebrate retina. Front Hum Neurosci *7*.

Warwick, R.A., Kaushansky, N., Sarid, N., Golan, A., and Rivlin-Etzion, M. (2018). Inhomogeneous Encoding of the Visual Field in the Mouse Retina. Curr Biol *28*, 655-+.

Wässle, H., Peichl, L., and Boycott, B.B. (1981). Morphology and Topography of on-Alpha and Off-Alpha Cells in the Cat Retina. Proc R Soc Ser B-Bio *212*, 157-175.

Williams, S.R. (2004). Spatial compartmentalization and functional impact of conductance in pyramidal neurons. Nat Neurosci *7*, 961-967.

Witkovsky, P. (2004). Dopamine and retinal function. Doc Ophthalmol *108*, 17-40.

Wood, S.N. (2006). Generalized additive models: an introduction with R (Boca Raton, Florida, U. S. A.: Chapman & Hall).

Yu, W.Q., El-Danaf, R.N., Okawa, H., Pacholec, J.M., Matti, U., Schwarz, K., Odermatt, B., Dunn, F.A., Lagnado, L., Schmitz, F*., et al.* (2018). Synaptic Convergence Patterns onto Retinal Ganglion Cells Are Preserved despite Topographic Variation in Pre- and Postsynaptic Territories. Cell Rep *25*, 2017-2026 e2013.

Yuste, R., and Denk, W. (1995). Dendritic Spines as Basic Functional Units of Neuronal Integration. Nature *375*, 682-684.

Zenisek, D., Henry, D., Studholme, K., Yazulla, S., and Matthews, G. (2001). Voltage-dependent sodium channels are expressed in nonspiking retinal bipolar neurons. Journal of Neuroscience *21*, 4543-4550.

9 Acknowledgement

To make this project work out, many people have engaged their great efforts in it. Therefore, I would like to thank:

- Prof. Dr. Thomas Euler for welcoming me to join such a creative lab and guiding me to work on this great project. I would like to thank him for all his guidance and supports given throughout these years, sharing his expertise and insights and sending me to wonderful international conferences and visiting other labs.
- Dr. Katrin Franke for all her guidance, patience and encouragements since I started my PhD. I would like to thank her also for her valuable suggestions, timely feedback, and contributions to this work.
- Prof. Dr. Philipp Berens and Prof. Dr. Tom Baden for all their suggestions, supports and contributions to this project.
- Dr. Timm Schubert for his guidance, discussion and suggestions during the past years.
- Prof. Dr. Frank Schaeffel and Prof. Dr. Aristides Arrenberg for being part of my advisory board and for their constructive feedback.
- Ziwei Huang for his great contributions to this project.
- Prof. Dr. Harald Baayen for advanced statistic help.
- Gordon Eske for technical support and for taking care of the mice.
- Valeska Botzenhardt for her help and patience.
- All members of the Euler, Franke and Berens groups for their feedback and creating a warm atmosphere in the lab. Especially, I would like to thank Michael Power for his help to correct mistakes in grammar as a native English speaker.

Finally, I would also like to thank my parents and my husband for their love, supports and encouragements during my whole PhD study.

10 Contributions

During my PhD study, I contributed to 3 studies. Two have been submitted and are available as a preprint at bioRxiv and the other one will be submitted soon. My contributions to each study are detailed below.

Manuscript #1

Ran Y*, Huang Z*, Baden T, Baayen H, Berens P, Franke K, Euler T (2019) Preprint: Type-specific dendritic integration in mouse retinal ganglion cells. bioRxiv 10.1101/753335.
*Authors contributed equally.
Currently under review at Nature Communications and is currently being revised for invited resubmission.

Contributions:
This study represents the main work I did during my PhD and the details are described in this thesis. In this work, we showed how different RGC types with similar inputs exhibited distinct spatio-temporal dendritic integration profiles, which highly tuned towards their specific visual computations. The computational modelling part, which was carried out by Ziwei Huang, suggest that dendritic morphology alone cannot explain the type-specific dendritic integration, instead, a combination of specific ion channels is required.

For this study, I performed all the experiments (i.e. single-cell injections and 2P imaging of light responses and cell morphologies), the pre-processing of functional and morphological data, the data analysis with respect to kinetic aspects of the cells' responses, as well as the morphological reconstructions and related analysis (with support from Ziwei Huang). In addition, wrote the first draft of the manuscript and contributed to and coordinated the editing of the manuscript up to the final version.

Manuscript #2

Szatko KP*, Korympidou MM*, Ran Y, Berens P, Dalkara D, Schubert S, Euler T, Franke K (2019)

Preprint: Neural circuits in the mouse retina support color vision in the upper visual field. bioRxiv 10.1101/745539.

*Authors contributed equally.

Manuscript was under review at Nature Communications and is currently being revised for invited resubmission.

Contributions:

Using two-photon imaging, this study showed that colour-opponent cells are predominantly located in the ventral retina across all retinal layers. This starts already at the level of the cone photoreceptor output, where colour-opponency is likely mediated by a rod-cone opponent pathway. The complexity of chromatic processing progressively increases towards the retinal output, where non-linear centre-surround interactions result in specific colour-opponent output channels to the brain.

For this study, I performed all electrophysiological single-cell patch-clamp recordings, which confirmed that the colour-opponency in the ventral retina observed via 2P imaging is likely not due to laser-mediated stimulation of the retina.

Manuscript #3

Le Chang*, Yanli Ran*, Olivia Auferkorte, Elisabeth Butz, Laura Hüser, Silke Haverkamp, Katrin Franke, Timm Schubert, Thomas Euler. Spike desensitisation as a mechanism for high-contrast selectivity in retinal ganglion cells. Manuscript in preparation.

*Authors contributed equally.

Contributions:

This study revealed that distinct spike generation mechanisms in On alpha and On *Igfbp5* RGCs underlie their specific light responses.

For this study, I performed some of the electrical single-cell patch-clamp recordings of On alpha cells. In addition, I contributed to the data analysis and helped editing the manuscript.